

Intraday Battery Dispatch for Hybrid Renewable Energy Assets

Thiha Aung and Mike Ludkovski

March 18, 2025

Abstract

We develop a mathematical model for intraday dispatch of co-located wind-battery energy assets. Focusing on the primary objective of firming grid-side actual production vis-a-vis the preset day-ahead hourly generation targets, we conduct a comprehensive study of the resulting stochastic control problem across different firming formulations and wind generation dynamics. Among others, we provide a closed-form solution in the special case of a quadratic objective and linear dynamics, as well as design a novel adaptation of a Gaussian Process-based Regression Monte Carlo algorithm for our setting. Extensions studied include an asymmetric loss function for peak shaving, capturing the cost of battery cycling, and the role of battery duration. In the applied portion of our work, we calibrate our model to a collection of 140+ wind-battery assets in Texas, benchmarking the economic benefits of firming based on outputs of a realistic unit commitment and economic dispatch solver.

Keywords: hybrid renewable assets, dynamic BESS dispatch, renewable generation firming, Gaussian process surrogates.

1 Introduction

Unlike conventional thermal generators that are fully dispatchable, variable renewable energy causes increased operational costs for power grids. Over- and under-generation requires deployment of regulation down/up reserves and is often associated with financial losses for the asset owner as well. Hybrid assets—defined as a “generating resource that is comprised of multiple generation or energy storage technologies controlled as a single entity behind a single point of interconnection” ([North American Electric Reliability Corporation, 2021](#))—have been gaining popularity as a means to mitigate the variability inherent to standalone renewable generation ([Ahlstrom et al., 2021](#)). According to [Gorman et al. \(2024\)](#) report, 46% of new renewable projects in the US listed in grid interconnection queues at the end of 2023 were of hybrid type, and total deployed hybrid capacity includes 49GW of renewable generation and 24.2 GWh of energy capacity, which is almost half of all deployed battery capacity in the US.

A hybrid resource combines a renewable energy source—most commonly solar or wind—with an energy storage system. We focus on fully hybrid resources that included both co-located and co-controlled resources that are treated as a single grid participant. Multiple storage technologies are being utilized (electrochemical battery storage, mechanical gravity, compressed air, electrical

capacitors, hydrogen fuel cells) with lithium-ion battery energy storage system (BESS) being the most common at present. Thanks to the controlled storage system, hybrid assets offer additional flexibility, closing the gap to traditional dispatchable generators. The comprehensive report by [Hybrid Resources Task Force \(2022\)](#) lists more than a half a dozen different drivers for resource hybridization, including avoided distribution and transmission upgrades, reduced curtailment, hedge against varying market conditions, and simplified procurement for utility generation off-takes. In turn, EIA ([US Energy Information Administration, 2024](#)) reports that hybrid resources utilize their batteries for many diverse use cases, from energy price arbitrage and ancillary service provision, to system peak shaving.

A critical use case of hybrid asset concerns renewable firming/curtailment mitigation in the sense of dispatching the battery to maximally match the hybrid output with an exogenous dispatch target. For example, this target can correspond to the day-ahead generation forecast employed by the system operator for security-constrained unit commitment. Firming objectives also arise naturally in the context of resource adequacy analysis and Power Purchase Agreements offtakes that reward predictability of generation.

In this paper we investigate operation of hybrid assets on operational time scales, focusing on optimal dispatch of the coupled BESS. To fix ideas, we consider wind-hybrid assets with our first task corresponding to the above firming objective. Thus, the BESS is dynamically controlled to counter the deviations of realized wind power output relative to a given dispatch target. Taking into account the intertemporal constraints of the BESS storage capacity and power rating limits, we study the resulting state-constrained finite-horizon stochastic optimal control problem.

Our developments span methodological, algorithmic and empirical aspects. Methodologically, we use a stochastic differential equation to directly model renewable energy generation and formulate a generic intra-day control problem for hybrid BESS dispatch. Starting with asset firming, we demonstrate its applicability for peak shaving and congestion/curtailment avoidance tasks. Moreover, we show that we can incorporate battery degradation control criteria into our flexible framework. Algorithmically, we directly implement the dynamic programming equation with state constraints by utilizing a simulation-based machine learning algorithm of Regression Monte Carlo (RMC)-type. Using actor-critic concepts we build two Gaussian Process emulators for the continuation-value and optimal control maps. Our algorithm is agnostic to assumed state dynamics which can be highly nonlinear and also agnostic to the objective function. We leverage two main features of the RMC: a statistical surrogate to approximate the q -function and a customized simulation design. We propose direct optimization of the control over the cost functional, which includes the q -value surrogate.

To provide empirical validation, we carry out a comprehensive case study, calibrating our model to realistic wind power production data from the synthetic Texas-7k transmission grid that is a digital twin of the Electric Reliability Council of Texas (ERCOT) grid. After fitting our probabilistic model for each wind unit in Texas-7k, we run grid-scale dispatch simulations to assess the impact of hybridization on asset firming and daily dispatch savings. Our simulations rely on actual (rather than model-based) wind and load profiles, providing an out-of-sample quantification of how well our dispatch algorithm performs in real-life conditions.

The literature on optimal operation of hybrid energy resources is still nascent and can be grouped in terms of the assumed control strategy types and objectives. Within the continuous-time stochastic

control paradigm, several studies treat similar problems using partial differential equation (PDE) methods. [Johnson, Howell, and Duck \(2017\)](#) assume a priori Bang-Bang control strategy for the control of BESS to track daily commitments over the 24-hour operating horizon. Their solution relies on approximation of the BESS constraints via boundary conditions and solving the Hamilton-Jacobi-Bellman (HJB) PDE numerically. [Collet, Féron, and Tankov \(2018\)](#) study the stochastic optimal control problem of a hybrid wind asset for energy arbitrage. The authors also assume a Bang-Bang control strategy for tracking dispatch targets and introduce a decision variable to perform energy arbitrage given the intraday price process. Unlike [Johnson et al. \(2017\)](#) and [Collet et al. \(2018\)](#), we focus on optimal control of BESS for tracking dispatch targets instead of the Bang-Bang principle and directly handle the constraints without approximations. Recent advances in deep learning via neural networks (NN) have been connected to stochastic control, in particular via probabilistic deep BSDE methods ([Han & Hu, 2020](#)) and the deterministic Deep Galerkin Method ([Sirignano & Spiliopoulos, 2018](#)) that globally approximates the nonlinear HJB PDE via neural networks. See [Bachouch, Huré, Langrené, and Pham \(2022\)](#) for a comprehensive study of NN-based algorithms that emulate value and control maps of the dynamic programming equations, including in the context of natural gas storage, and [Abi Jaber et al. \(2024\)](#) and [Bermúdez and Padín \(2024\)](#) for optimizing intraday trading/energy arbitrage.

[Belloni, Piroddi, and Prandini \(2016\)](#) treat hybrid asset firming using Approximate Dynamic Programming. However, their modeling is limited to linear dynamics of BESS and wind, with linear performance criterion and discretization of the wind process, whereas our algorithm works directly with a continuous state space. As alternative control frameworks, Model Predictive Control ([Khalid & Savkin, 2010](#); [van der Meer et al., 2021](#); [Kou et al., 2015](#)) and scenario-based stochastic programming ([Oskouei & Yazdankhah, 2015](#); [Ding et al., 2012](#)) have also been applied to BESS operation in hybrid renewable energy systems.

Beyond hybrid configurations, BESS is widely utilized for standalone applications, including energy arbitrage in real-time and/or day-ahead markets ([Zheng et al., 2023](#)), as well as participation in ancillary service markets ([Arteaga & Zareipour, 2019](#); [He et al., 2016](#); [Krishnamurthy et al., 2018](#); [Wu et al., 2015](#)). Another important aspect of BESS dispatch is accounting for battery degradation. The standard rainflow cycle counting technique ([Muenzel et al., 2015](#)) connects battery degradation to the depth of charge and discharge. Incorporating rainflow counting within a stochastic control formula is challenging due its path-dependent nature. Existing solutions include adding additional state variables to track charging and discharging cycles in order to make a linear-quadratic approximation of degradation costs ([Koller et al., 2013](#); [Lee & Kim, 2022](#)).

To tackle our stochastic control problem, we extend the Stochastic Hybrid Asset Dispatch Optimization with Gaussian Processes (SHADoW-GP) algorithm, developed in our previous work [Aung and Ludkovski \(2024\)](#). The algorithm involves a direct implementation of the dynamic programming equations via machine learning, namely by building two GP emulators for the continuation-value and the optimal control maps. Compared to neural networks, GPs have higher sample efficiency, requiring significantly fewer training samples to achieve accurate approximations. We refer to [Ludkovski and Maheshwari \(2020\)](#); [Alasseur et al. \(2019\)](#); [Balata et al. \(2021\)](#) for other applications of GPs in stochastic optimal control for renewable energy management.

[Aung and Ludkovski \(2024\)](#) focused on algorithm development, exploring how GP emulators

can be applied to solve a hybrid wind-storage control problem, but with simplified and less realistic modeling assumptions. The numerical experiments relied on time-stationary mean-reverting dynamics and utilized quadratic objective. In contrast, this work targets realistic modeling and algorithm deployment. To this end, to account for wind generation constraints we utilize the time-dependent Jacobi-type SDE and extend to non-Gaussian noise process. Similarly, we consider a range of nonlinear objectives, including bang-bang control, curtailment mitigation, and degradation-aware optimization. We also present a novel theoretical result by deriving an analytical solution for the optimal control of BESS under “soft” state-of-charge constraints.

Summary of Contributions: Our paper presents a comprehensive and innovative study on the optimal intra-day dispatch of hybrid renewable resources under a range of performance criteria. We directly work with probabilistic, time- and forecast-dependent generation scenarios, continuous input and action spaces. From an experimental perspective, we provide a quantitative assessment of the gains from retrofit hybridization of wind assets in a realistic grid dispatch test-bed.

The rest of the paper is organized as follows. Section 2 presents the stochastic optimal control problem set-up for the hybrid asset. A linear quadratic approximation of the constraints and analytical solution is discussed in Section 2.4. In Section 3, we present our SHADOW-GP algorithm. Section 4 is devoted to an extended case study of hybridizing wind assets in the synthetic Texas-7k grid. Results on additional optimization objectives are provided in Section 5. Section 6 outlines future research directions.

2 Problem Formulation

We consider a standard probability space $(\Omega, \mathcal{F}, (\mathcal{F}_t)_{t \in [0, T]}, \mathbb{P})$. We work with two Markovian state variables: the exogenous wind generation process $(X_t)_{t \in [0, T]}$ and the controlled State of Charge (SoC) process $(I_t)_{t \in [0, T]}$, both adapted to the filtration $\mathbb{F} = (\mathcal{F}_t)_{t \in [0, T]}$. The SoC process is controlled by the charge/discharge rate process $(B_t)_{t \in [0, T]}$, a continuous \mathbb{F} -adapted decision variable. The BESS is dynamically controlled throughout the 24-hour operation period as (X_t) evolves, subject to control and state constraints of the SoC process. This is interpreted as real-time adjustment by the hybrid asset owner; note that we are not referencing any power prices or bidding/auctions.

2.1 Wind Power Generation Dynamics

Denote by $X = (X_t)_{t \in [0, T]}$ the wind power generation process on the operating horizon $[0, T]$ in units MW. In continuous time, we utilize a mean-reverting stochastic differential equation (SDE) for (X_t) . The mean reversion level can be interpreted as the day-ahead forecast $(m_t)_{t \in [0, T]}$ and the diffusion term captures the real-time generation uncertainty. Because generation is non-negative and capped by the nameplate generation capacity, the domain of X is bounded, $X_t \in [0, X_{\max}]$. To capture all the above features, we work with Jacobi diffusion SDEs (Møller et al., 2016; Caballero et al., 2021)

$$dX_t = \alpha_t(m_t - X_t) dt + \sigma_t \sqrt{X_t(X_{\max} - X_t)} dW_t, \quad X_0 = x_0, \quad (1)$$

where $\sigma_t > 0$ is the volatility parameter, $\alpha_t > 0$ is the dimensionless mean-reversion parameter, and $(W_t)_{t \in [0, T]}$ is a Wiener process. Note that the mean reversion rate α_t and the volatility σ_t are

time-dependent to capture the diurnal variability in wind power output.

Remark 1. *A similar modeling applies to hybrid PV (photovoltaic) + battery storage or hybrid PV+wind+battery storage systems. However, unlike wind, solar generation is constrained by daylight hours, meaning the temporal domain of non-zero (X_t) would be restricted to a subset of $[0, T]$. Moreover, while there is widespread adoption of BESS to co-locate with solar farms, the primary goal is to shift generation to the evening/early morning hours rather than the firming objective that is our focus herein.*

2.2 Storage Dynamics

Let $I = (I_t)_{t \in [0, T]}$ represent the SoC of the hybrid BESS over the operating horizon $[0, T]$. The SoC process quantifies the stored energy in MWh and is taken to be Markovian, subject to charge/discharge rate constraints and capacity constraints. The dynamics of I is given by:

$$dI_t = \left(\eta B_t \mathbb{1}_{\{B_t > 0\}} + \frac{1}{\eta} B_t \mathbb{1}_{\{B_t < 0\}} \right) dt, \quad I_0 = \iota, \quad (2)$$

where B_t is the controlled charge/discharge rate in MW at time t and $0 < \eta \leq 1$ is the dimensionless charge/discharge efficiency parameter. Positive $B_t > 0$ denotes charging, while $B_t < 0$ represents discharging, so that η captures charging inefficiencies, which means that the battery dissipates more energy than it discharges and accumulates less energy than it charges (Collet et al., 2018; van der Meer et al., 2021; Kordonis et al., 2023). Typical values for η are around 90-95%.

The state-of-charge bounds are given by the battery capacity constraints:

$$I_{\min} \equiv \text{SoC}_{\min} \cdot I_{\text{cap}} \leq I_t \leq \text{SoC}_{\max} \cdot I_{\text{cap}} \equiv I_{\max}, \quad (3)$$

where I_{cap} is the rated battery capacity in MWh and $0 \leq \text{SoC}_{\min} < \text{SoC}_{\max} \leq 1$ are SoC limits. Typical values for the latter are $\text{SoC}_{\min} = 0.05, \text{SoC}_{\max} = 0.95$. The BESS power rating is characterized by $B_{\max} > 0$ and $B_{\min} < 0$ that restrict the range of the control B_t :

$$B_{\min} \leq B_t \leq B_{\max}. \quad (4)$$

The Markovian structure of (X_t, I_t) allows us to express the optimal control of the stochastic control problem in feedback form $B_t = \Psi(t, X_t, I_t)$ and adapted to filtration \mathbb{F} .

2.3 Stochastic Control Problem

A hybrid asset engages in grid dispatch by receiving dispatch signals $(M_t)_{t \in [0, T]}$ from the Independent System Operator (ISO). During operation, the realized power output X_t deviates from the dispatch target M_t and the hybrid asset charges/discharges the battery so that the net output

$$O_t := X_t - B_t$$

is close to M_t . That is, the BESS agent dynamically decides the dispatch rate in MW as a function of the SoC and the wind power output; see Figure 1.

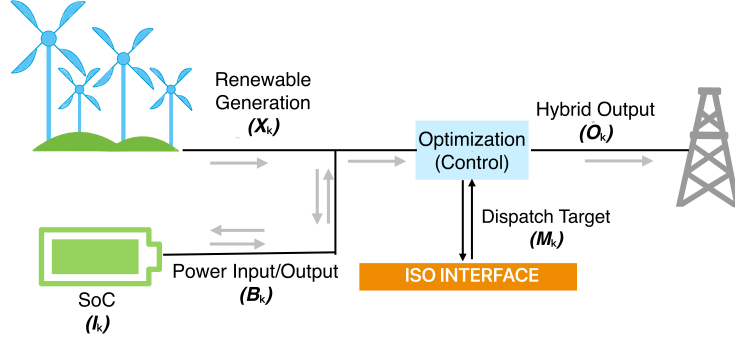


Figure 1: A schematic description of optimizing the output (O_k) of a hybrid wind asset.

Mathematically, denote by $X^{t,x} = (X_s^{t,x})_{s \in [t,T]}$ the solution of the SDE (1) starting from x at t and by $I^{B;t,\iota} = (I_s^{B;t,\iota})_{s \in [t,T]}$ the solution of the SoC process (2), starting from ι , and controlled by $B := (B_s)_{s \in [t,T]}$. Let $\mathcal{B}(t, x, \iota)$ be the set of feasible controls for that initial condition:

$$\mathcal{B}(t, x, \iota) = \{B : B_s \text{ is } \mathcal{F}_s\text{-adapted, } B_{\min} \leq B_s \leq B_{\max}, I_{\min} \leq I_s \leq I_{\max}, \forall s \in [t, T]\}. \quad (5)$$

We consider the stochastic control problem with value function $V : [t, T] \times \mathcal{D} \rightarrow \mathbb{R}$:

$$V(t, x, \iota) := \inf_{B \in \mathcal{B}(t, x, \iota)} \mathbb{E} \left[\int_t^T f(X_s^{t,x}, B_s, M_s) ds + g(I_T^{B;t,\iota}) \right], \quad (6)$$

where the domain is the bounded set $\mathcal{D} := \mathcal{X} \times \mathcal{I} \subset \mathbb{R}^2$ with $\mathcal{X} = [0, X_{\max}]$ and $\mathcal{I} = [I_{\min}, I_{\max}]$. The running cost f represents the stepwise performance criterion for optimal BESS dispatch over the interval $[0, T]$ which depends on the target M_t . The motivating stepwise cost is a quadratic firming criterion

$$\tilde{f}(X, B, M) := (X - B - M)^2. \quad (7)$$

The terminal cost function $g(I_T)$ captures the final SoC level that the BESS needs to end up at to be ready for the next operational day.

Remark 2. *The natural firming target would be $M_t = \mathbb{E}[X_t]$ which is different from the mean-reversion level m_t as the dynamics of (X_t) are time-dependent.*

2.4 Explicit Solution via Linear-Quadratic Approximation

To set a baseline for latter developments, we first consider a linearized setup that admits an explicit solution. To this end, we cast (6) into the linear-quadratic framework and then analytically solve the corresponding HJB equation.

Dynamic programming (Pham, 2009) suggests that the value function of (6) can be characterized as the viscosity solution of the HJB PDE

$$\partial_t V + \inf_{b \in \mathcal{B}_t} \left\{ \alpha_t (m_t - x) \partial_X V + (\eta b \mathbb{1}_{\{b > 0\}} + \frac{1}{\eta} b \mathbb{1}_{\{b < 0\}}) \partial_I V + \frac{1}{2} \sigma_t^2 x (X_{\max} - x) \partial_{XX} V + f(x, b, M_t) \right\} = 0, \quad (8)$$

where $(x, \iota) \in \mathcal{D}$ with terminal condition $V(T, x, \iota) = g(\iota)$. Above,

$$\mathcal{B}_t := [B_{\min} \cdot \mathbb{1}_{I_t > I_{\min}}, B_{\max} \cdot \mathbb{1}_{I_t < I_{\max}}] \quad (9)$$

denotes the I_t -dependent admissible charge/discharge rates at time t . To solve our problem analytically, we relax the hard constraints in \mathcal{B}_t using a quadratic penalty on the state and control variables. Furthermore, we take a quadratic terminal cost and linearize the dynamics of I_t :

- Linear dynamics for the SoC process by considering $\eta = 1$ (100% efficient) BESS:

$$dI_t = B_t dt, \quad I_0 = \iota, \quad (10)$$

- Quadratic stepwise cost \bar{f} , with the firming criterion modified to include an approximation of the hard state and control constraints with penalties $c_1, c_2 > 0$:

$$\bar{f}(X_t, B_t, M_t, I_t) = \tilde{f}(X_t, B_t, M_t) + c_1 B_t^2 + c_2 (I_t - I_m)^2 \quad (11)$$

where $I_m := \frac{I_{\max} - I_{\min}}{2}$.

- A quadratic terminal penalty centered around a target SoC level I_{target} :

$$\bar{g}(I_T) = \mathcal{P} \cdot (I_T - I_{\text{target}})^2 \quad \text{with} \quad \mathcal{P} > 0. \quad (12)$$

Under the above assumptions, we obtain an HJB PDE with unconstrained real-valued control set:

$$\begin{aligned} \partial_t \bar{V} + \inf_{\bar{b} \in \mathbb{R}} \left\{ \alpha_t (m_t - x) \partial_X \bar{V} + \bar{b} \partial_I \bar{V} + \frac{1}{2} \sigma_t^2 x (X_{\max} - x) \partial_{XX} \bar{V} \right. \\ \left. + (x - \bar{b} - M_t)^2 + c_1 \bar{b}^2 + c_2 (\iota - I_m)^2 \right\} = 0 \end{aligned} \quad (13)$$

with terminal condition $V(T, x, \iota) = \bar{g}(\iota)$.

Proposition 1. *Assume that the solution \bar{V} of (13) is $\mathcal{C}^{1,2}([0, T] \times \mathcal{D})$. Given a constant mean-reversion level of the wind SDE, $m_t = m \forall t \in [0, T]$, the value function is quadratic in its arguments and is given by:*

$$\begin{aligned} \bar{V}(t, x, \iota) = P_1(t)(\iota - I_m)^2 + P_2(t)(\iota - I_m)(x - m) + P_3(t)(x - m)^2 \\ + P_4(t)(\iota - I_m) + P_5(t)(x - m) + P_6(t), \end{aligned} \quad (14)$$

where the functions P_1, \dots, P_6 solve the system of backward Riccati ordinary differential equations

$$\begin{cases} \dot{P}_1(t) + c_2 - \kappa(P_1(t))^2 = 0, & P_1(T) = \mathcal{P} \\ \dot{P}_2(t) - \alpha_t P_2(t) - \kappa P_1(t) P_2(t) + 2\kappa P_1(t) = 0, & P_2(T) = 0 \\ \dot{P}_3(t) + (1 - \kappa) - (2\alpha_t + \sigma_t^2) P_3(t) + \kappa P_2(t) - \frac{\kappa}{4} (P_2(t))^2 = 0, & P_3(T) = 0 \\ \dot{P}_4(t) + 2\kappa(m - M_t) P_1(t) - \kappa P_1(t) P_4(t) = 0, & P_4(T) = 2\mathcal{P}(I_m - \iota_{\text{target}}) \\ \dot{P}_5(t) + 2(1 - \kappa)(m - M_t) - \alpha_t P_5(t) + \kappa P_4(t) + \kappa(m - M_t) P_2(t) \\ \quad - \frac{\kappa}{2} P_2(t) P_4(t) + (\sigma_t^2 X_{\max} - 2\sigma_t^2 m) P_3(t) = 0, & P_5(T) = 0 \\ \dot{P}_6(t) + (1 - \kappa)(m - M_t)^2 + \kappa(m - M_t) P_4(t) - \frac{\kappa}{4} (P_4(t))^2 = 0, & P_6(T) = \mathcal{P}(I_m - \iota_{\text{target}})^2 \end{cases} \quad (15)$$

where $\kappa = \frac{1}{1+c_1}$.

Moreover, the optimal control in (13) is of the closed-loop feedback form and is given by:

$$\bar{b}(t, x, \iota) = \kappa(x - M_t) - \kappa P_1(t)(\iota - I_m) - \frac{\kappa}{2} P_2(t)(x - m) - \frac{\kappa}{2} P_4(t). \quad (16)$$

The proof of Proposition 1 is provided in Appendix A. The proof relies on solving a quadratic ansatz for (13). We remark that while linear-quadratic HJB equations have appeared in many settings in the literature, Proposition 1 is non-standard because our stochastic state follows the nonlinear (but affine, which is the property necessary for the ansatz) Jacobi SDE (1). Moreover, we provide the solution for the general case of time-dependent coefficients, arbitrary deterministic target (M_t) and arbitrary I_0 .

3 Numerical Algorithm

In this section, we present an algorithm to solve the stochastic control problem (6) for general piecewise-linear SoC dynamics with hard constraints. The algorithm is presented in discrete time with step size Δt , such that $T = K\Delta t$. Denoting the time index at $t_k = k\Delta t$ with subscript k , the discrete-time versions of the wind generation and BESS dynamics are

$$X_{k+1} = X_k + \alpha_k(m_k - X_k)\Delta t + \sigma_k \sqrt{X_k(X_{\max} - X_k)} \sqrt{\Delta t} \cdot Z_k, \quad Z_k \sim \mathcal{N}(0, 1); \quad (17)$$

$$I_{k+1} = I_k + (\eta B_k \mathbb{1}_{\{B_k > 0\}} + \frac{1}{\eta} B_k \mathbb{1}_{\{B_k < 0\}}) \Delta t. \quad (18)$$

We rely on RMC-type algorithm which exploits the Dynamic Programming Principle (DPP). The Bellman equation between t_k and t_{k+1} is given by:

$$V(t_k, X_k, I_k) = \inf_{B_k \in \mathcal{B}_k(I_k)} \left\{ f(X_k, B_k, M_k) \Delta t + \mathbb{E}[V(t_{k+1}, X_{k+1}, I_{k+1}) | X_k, I_k] \right\} \quad (19)$$

where $\mathcal{B}_k(I_k)$ is the discrete-time counterpart of the admissible control set (9) for B_k , adjusted to make sure that I_{k+1} in (18) will remain within $[I_{\min}, I_{\max}]$:

$$\mathcal{B}_k(I_k) := \{B_k \in \mathbb{R} : B_{\min}(I_k) \leq B_k \leq B_{\max}(I_k)\} \quad (20)$$

where

$$B_{\min}(I_k) := \max \left(B_{\min}, \frac{\eta \cdot (I_{\min} - I_k)}{\Delta t} \right), \quad B_{\max}(I_k) := \min \left(B_{\max}, \frac{I_{\max} - I_k}{\eta \Delta t} \right).$$

The expectation in (19) is taken over the random variable X_{k+1} , conditioned on current wind power output X_k . In line with the DPP approach, we define the cost-to-go q -value

$$Q(t_k, X_k, I_{k+1}) := \mathbb{E} \left[V(t_{k+1}, X_{k+1}, I_{k+1}) \mid X_k \right] \quad (21)$$

and characterize the optimal control at step t_k via

$$B_k^*(X_k, I_k) := \arg \inf_{B_k \in \mathcal{B}_k(I_k)} \left\{ f(X_k, B_k, M_k) \Delta t + Q(t_k, X_k, I_k + (\eta B_k \mathbb{1}_{\{B_k > 0\}} + \frac{1}{\eta} B_k \mathbb{1}_{\{B_k < 0\}}) \Delta t) \right\}. \quad (22)$$

To solve (22) we approximate $Q(t_k, \cdot, \cdot)$ using a machine learning model.

3.1 SHADOW-GP Algorithm

The key idea is to fit the q -value $Q(t_k, \cdot, \cdot)$ via a statistical emulator \hat{Q}_k for each k , such as Linear Regression, Decision Trees, or Gaussian Process Regression (Ludkovski & Maheshwari, 2020). The fitting is done based on an empirical regression using the training set, termed the simulation design, \mathcal{D}_k^v of size N . Note that since the q -value \hat{Q}_k is a function of the *current* wind power generation X_k at step t_k and the *lookahead* SoC I_{k+1} at step t_{k+1} , the simulation design is $\mathcal{D}_k^v = (X_k^n, I_{k+1}^n)_{n=1}^N$.

In our approach, we numerically optimize BESS dispatch at each input. To avoid repeated calls of optimization subroutines for the N training samples in \mathcal{D}_k^v during training and later for the post-training simulations, we also construct an emulator, \hat{B}_k , for the control map. Since \hat{B}_k is a feedback map of *current* wind generation X_k and *current* SoC I_k , the respective simulation design is $\mathcal{D}_k^b = (X_k^{b,n}, I_k^{b,n})_{n=1}^{N_b}$ of size N_b and distinct from \mathcal{D}_k^v . This results in an actor-critic scheme as described in Bachouch et al. (2022).

Following the standard DPP procedure, we proceed backward in time, starting with the known terminal condition $\hat{Q}_{K-1}(X_{K-1}, \iota) = g(\iota)$. For $k = K - 1, \dots, 0$, we repeat the following 6 steps:

- 1) Generate design spaces $\mathcal{D}_{k-1}^v = (X_{k-1}^n, I_k^n)_{n=1}^N$ and $\mathcal{D}_k^b = (X_k^{b,n}, I_k^{b,n})_{n=1}^{N_b}$;
- 2) Evaluate the pointwise optimal control $b_k^{*,n}$ for each input $(X_k^{b,n}, I_k^{b,n})$, $n = 1, \dots, N_b$ in \mathcal{D}_k^b according to (22) using a numerical optimizer;
- 3) Construct the policy map emulator $\hat{B}_k : (X, I) \mapsto \mathcal{B}_k \subset \mathcal{R}$ by regressing $b_k^{*,n}$ against design \mathcal{D}_k^b , i.e., an empirical L^2 -projection into the given function space \mathcal{H}^b ,

$$\hat{B}_k(\cdot) = \arg \inf_{h_k \in \mathcal{H}^b} \sum_{n=1}^{N_b} \left(h_k(X_k^{b,n}, I_k^{b,n}) - b_k^{*,n} \right)^2; \quad (23)$$

- 4) Perform a one-step forward simulation of \mathcal{D}_{k-1}^v : $X_{k-1}^n \mapsto X_k^n$ for $n = 1, \dots, N$;
- 5) Evaluate the pointwise value function in (19) for each (X_k^n, I_k^n) using the control $\hat{b}_k^n = \hat{B}_k(X_k^n, I_k^n)$ based on the above emulator $\hat{B}_k(\cdot)$:

$$v_k^n = f(X_k^n, \hat{b}_k^n, M_k) \Delta t + \hat{Q}_k(X_k^n, I_k^n + (\eta \hat{b}_k^n \mathbb{1}_{\{\hat{b}_k^n > 0\}} + \frac{1}{\eta} \hat{b}_k^n \mathbb{1}_{\{\hat{b}_k^n < 0\}}) \Delta t), \quad n = 1, \dots, N; \quad (24)$$

- 6) Construct the q -value emulator for

$$\hat{Q}_{k-1} : (X, I) \mapsto \mathbb{E}[\hat{V}(t_k, X_k, I) \mid X_{k-1} = X] \quad (25)$$

by regressing $v_k^{1:N}$ against the design \mathcal{D}_{k-1}^v within the function space \mathcal{H}^q :

$$\hat{Q}_{k-1}(\cdot) = \arg \inf_{q_{k-1} \in \mathcal{H}^q} \sum_{n=1}^N (q_{k-1}(X_{k-1}^n, I_k^n) - v_k^n)^2. \quad (26)$$

Note that at final step $k = 0$, once we train the control emulator $\hat{B}_k(\cdot)$, the training loop is complete and steps 4–6 involving the design \mathcal{D}_{k-1}^v are skipped. In the subsequent sections, we delve deeper into our selection of simulation design, q -value emulator, and control emulator.

Remark 3. An alternative is to directly fit the value function V instead of the continuation-value map Q (Bachouch et al., 2022). From an optimization perspective, such techniques solve a parameterized approximation of the value map and the policy map, rather than the optimization problem in (22).

3.2 Simulation Design

To perform the numerical optimization in step 2) above, we first need to generate the bi-variate simulation design \mathcal{D}_k^v at each time t_k . The regression emulator $\hat{Q}_k(\cdot)$ will be more accurate in regions with many samples and worse in regions with few samples. This necessitates a simulation design with thorough coverage. The standard space-filling approach is to take $(X_k^n, I_{k+1}^n) \sim \text{Unif}([X_{\min}, X_{\max}] \times [I_{\min}, I_{\max}])$. However, uniform i.i.d. samples tend to cluster, resulting in higher variance of the emulator. To avoid this issue, we rely on Latin Hypercube Sampling (LHS) to pick our design sites. Unlike Reinforcement Learning which generates the sampling domain via exploration-exploitation approach, we have a user-determined training domain, so that we must specify the range of \mathcal{D}_k^v . Ideally, at each timestep t_k , we should concentrate on the region that reflects the likely support of the random variables I_{k+1}^* and X_k . While X_k is exogenous, I_{k+1}^* is controlled by B_k^* . To this end, we space fill over the training domain $[X_{\min}^k, X_{\max}^k] \times [I_{\min}, I_{\max}]$, where the choice of X_{\min}^k and X_{\max}^k is taken as three times the standard deviation $\text{StDev}(X_k)$.

To enhance stability of the estimation of $\hat{Q}_k(\cdot)$, we rely on **replication**, dividing our training design into N_{loc} distinct sites, with each distinct input repeated N_{rep} times (for the remainder of the subsection, $\mathbf{x} \equiv (X, I)$ denotes a generic training input):

$$\mathcal{D}_k^v = \left\{ \underbrace{\mathbf{x}^{1,1}, \dots, \mathbf{x}^{1,N_{rep}}}_{N_{rep} \text{ times}}, \underbrace{\mathbf{x}^{2,1}, \dots, \mathbf{x}^{2,N_{rep}}}_{N_{rep} \text{ times}}, \dots, \underbrace{\mathbf{x}^{N_{loc},1}, \dots, \mathbf{x}^{N_{loc},N_{rep}}}_{N_{rep} \text{ times}} \right\}. \quad (27)$$

The total simulation budget at each step k is thus $|\mathcal{D}_k^v| = N_{loc} \times N_{rep}$. Subsequently, one-step forward simulations and evaluations are performed to acquire the respective responses $v^{1,1}, \dots, v^{i,j}, \dots, v^{N_{loc},N_{rep}}$. Denote by

$$\bar{\mathcal{D}}_k^v = \{\mathbf{x}^1, \mathbf{x}^2, \dots, \mathbf{x}^{N_{loc}}\} \quad (28)$$

the design \mathcal{D}_k^v without replicates, i.e., $\bar{\mathcal{D}}_k^v$ contains just the N_{loc} unique training X -values. After pre-averaging the responses of each replicated batch $\bar{v}^n := \frac{1}{N_{rep}} \sum_{j=1}^{N_{rep}} v^{n,j}$, the regression model for the continuation value emulator $\hat{Q}_k(\cdot)$ is constructed by regressing $\bar{v}^{1:N_{loc}}$ against the design $\bar{\mathcal{D}}_k^v := (\mathbf{x}^{1:N_{loc}})$. Mathematically speaking, the pre-averaging is equivalent to a Monte Carlo approximation of conditional expectation in (21). The replicated design lowers regression training errors thanks to the decreased variability in \bar{v}^n 's, raising the signal-to-noise ratio.

We similarly use LHS to generate the training design $\mathcal{D}_k^b = (X_k^{b,n}, I_k^{b,n})_{n=1}^{N_b}$ for $\hat{B}_k(\cdot)$, covering the same domain as \mathcal{D}_k^v . Since the optimal control values (22) do not depend on forward simulations, \mathcal{D}_k^b does not require replicates.

Remark 4. *To ensure the existence of samples at the minimum SoC I_{\min} and the maximum SoC I_{\max} , we add additional training inputs at $I = I_{\min}^{k+1}$ and $I = I_{\max}^{k+1}$. Similarly, we opt for additional training points at $X = X_{\min}^k$ and $X = X_{\max}^k$. That is, we deploy a **fencing** mechanism by creating an additional layer of (evenly spaced) training inputs on the boundary of the sampling domain $[X_{\min}^k, X_{\max}^k] \times [I_{\min}^{k+1}, I_{\max}^{k+1}]$ prior to replication, see Figure 5 below.*

3.3 Gaussian Process Emulator for Q

In order to enhance the numerical optimization of B_k^* in (22), we opt for an emulator that has an analytical gradient. To achieve this, we make use of Gaussian Process regression (GPR).

GPR models $Q_k(\cdot)$ as a Gaussian Process specified by a mean function $m(\mathbf{x})$ (taken to be zero after standardizing the outputs) and positive definite covariance function $c(\mathbf{x}, \mathbf{x}'; \vartheta)$ (Rasmussen & Williams, 2006). The hyperparameters ϑ of the covariance kernel $c(\cdot, \cdot)$ specify the smoothness of \hat{Q} . Given a training design $(\mathbf{x}^{1:N}, v^{1:N})$ and an input \mathbf{x}^* , the continuation value, $\hat{Q}(\mathbf{x}^*)$, is the posterior mean of the GP given by

$$\hat{Q}(\mathbf{x}_*) = \mathcal{C}_*^\top (\mathbf{C} + \sigma_\epsilon^2 \mathbf{I})^{-1} \mathbf{v} \quad (29)$$

where \mathbf{I} is $N \times N$ identity matrix, $\mathbf{v} = [v^1, \dots, v^N]^\top$, and the vector \mathcal{C}_* is

$$\mathcal{C}_*^\top = [c(\mathbf{x}_*, \mathbf{x}^1; \vartheta), \dots, c(\mathbf{x}_*, \mathbf{x}^N; \vartheta)]. \quad (30)$$

Here, σ_ϵ^2 represents observation noise and \mathbf{C} is the $N \times N$ covariance matrix with $\mathbf{C}_{k,l} = c(\mathbf{x}_k, \mathbf{x}_l; \vartheta)$. One may opt for different kernels, see Rasmussen and Williams (2006). In our study, we choose the twice-differentiable anisotropic Matérn-5/2 kernel with three hyperparameters $\vartheta = (\sigma_p^2, \ell_1, \ell_2)$

$$c_{M52}(\mathbf{x}, \mathbf{x}'; \vartheta) := \sigma_p^2 \prod_{j=1}^2 \left(1 + \frac{\sqrt{5}}{\ell_j} |x_j - x'_j| + \frac{5}{3\ell_j^2} (x_j - x'_j)^2 \right) \cdot \exp\left(-\frac{\sqrt{5}}{\ell_j} |x_j - x'_j|\right), \quad (31)$$

where σ_p^2 indicates the magnitude of the response, and ℓ_1 and ℓ_2 determine how the response fluctuates with respect to wind power generation (MW) and SoC (MWh), which are expressed in different scales and units and hence have different lengthscales. In simple terms, a large lengthscale suggests a smooth response surface, while a small lengthscale indicates a non-smooth surface with significant fluctuations. The hyperparameters ϑ and σ_ϵ^2 are optimized using the maximum likelihood estimation (MLE) method. To accelerate GP $\hat{Q}_k(\cdot)$ optimization at step k , we warm-start with the hyperparameters $\vartheta^{(k+1)}$ obtained from the trained GP $\hat{Q}_{k+1}(\cdot)$ at step $k+1$. We also standardize both inputs and outputs in the range $[-1, 1]$ to improve the numerical stability of the GP MLE step.

Remark 5. *We emphasize the practical effectiveness of batching inputs; using replicates not only dramatically speeds up GPR training time which is cubic in N_{loc} but moreover offers more stable MLE results thanks to lower observation noise.*

3.4 Gaussian Process emulator for B

The constrained optimization problem in (22) is given implicitly in terms of the emulator $\hat{Q}_k(\cdot)$, with the respective first-order-condition tied to $\partial \hat{Q}_k / \partial I$. GP allows the use of faster gradient-based optimizers thanks to its analytical gradients. Differentiating the GP $\hat{Q}(\cdot)$ with Matérn-5/2 kernel in x_j gives another GP with posterior mean at input \mathbf{x}_* given by

$$\frac{\partial \hat{Q}}{\partial x_j}(\mathbf{x}_*) = \sum_{n=1}^N \alpha_n \frac{\partial c_{M52}}{\partial x_j}(\mathbf{x}_*, \mathbf{x}^n; \vartheta), \quad (32)$$

where α_n is the n -th component of $(\mathbf{C} + \sigma_\epsilon^2 \mathbf{I})^{-1} \mathbf{v}$ and

$$\frac{\partial c_{M52}}{\partial x_j}(\mathbf{x}_*, \mathbf{x}; \vartheta) = c_{M52}(\mathbf{x}_*, \mathbf{x}; \vartheta) \cdot \frac{-\frac{5}{3\ell_j^2} r_j - \frac{5^{3/2}}{3\ell_j^3} r_j |r_j|}{1 + \frac{\sqrt{5}}{\ell_j} |r_j| + \frac{5}{3\ell_j^2} (r_j)^2}, \quad (33)$$

with $r_j = (x_j - x_j^*)$. In our case, we utilize the gradient with respect to SoC, $j = 2$ in (33). The presence of the black-box \hat{Q} makes the optimization problem non-convex. Since we have one-dimensional control, we project the constraints onto the optimal control solution from the unconstrained case. We employ the unconstrained, gradient-based **L-BFGS** solver from the **SciPy** library to retrieve optimized outputs without constraints. That is, instead of solving for (22) with $\hat{Q}_k(\cdot)$ directly, we instead solve:

$$B_k^\dagger(X_k, I_k) := \arg \inf_{B_k \in \mathbb{R}} \left\{ f(X_k, B_k, M_k) \Delta t + \hat{Q}_k(X_k, I_k + (\eta B_k \mathbb{1}_{\{B_k > 0\}} + \frac{1}{\eta} B_k \mathbb{1}_{\{B_k < 0\}}) \Delta t) \right\} \quad (34)$$

As an alternative, we can directly solve for the root of the first-order condition of (34). When the cost function is given by $f(X_k, B_k, M_k) = (X_k - M_k - B_k)^2$, the first-order condition for the optimal B_k^\dagger is:

$$2(X_k - M_k - B_k^\dagger) = \begin{cases} \eta \frac{\partial \hat{Q}_k}{\partial I}(B_k^\dagger), & B_k^\dagger > 0, \\ \frac{1}{\eta} \frac{\partial \hat{Q}_k}{\partial I}(B_k^\dagger), & B_k^\dagger < 0, \\ 0, & B_k^\dagger = 0. \end{cases} \quad (35)$$

Using the analytical gradient of the GP, $\frac{\partial \hat{Q}_k}{\partial I}$, we can apply a root-finding algorithm to (35) to determine B_k^\dagger . Then, we directly enforce the constraints that define the feasible set \mathcal{B}_k onto $B_k^\dagger(X_k, I_k)$ to obtain the optimal pointwise control $B_k^*(X_k, I_k)$ in (22).

Emulating the feedback control map: The unconstrained optimization with manual projection in (34) serves two purposes: saving training time compared to constrained optimization and construction of the emulator for $\hat{B}_k(\cdot)$. Directly building an emulator over the output $B_k^*(X_k, I_k)$ with hard constraints does not guarantee feasibility. This is still an active area of research (Kotary et al., 2021; Kotary & Fioretto, 2024; Donti et al., 2021). To guarantee feasibility, we train \hat{B}_k by regressing *unconstrained* optimized $(b_k^{\dagger, n})_{n=1}^{N_b}$ against $\mathcal{D}_k^b = (X_k^{b, n}, I_k^{b, n})_{n=1}^{N_b}$ with a projection layer onto feasible set \mathcal{B}_k post-training. The equation for \hat{B}_k (23) becomes

$$\check{B}_k(\cdot) = \arg \inf_{h_k \in \mathcal{H}^b} \sum_{n=1}^{N_b} \left(h_k \left(X_k^{b, n}, I_k^{b, n} \right) - b_k^{\dagger, n} \right)^2; \quad (36)$$

$$\hat{B}_k(X_k^{b, n}, I_k^{b, n}) = \text{Proj}_{\mathcal{B}_k(I_k^{b, n})} \{ \check{B}_k(X_k^{b, n}, I_k^{b, n}) \}, \quad (37)$$

where the projection depends pointwise on $I_k^{b, n}$. To fit \check{B}_k , we rely on GP with a Matérn-3/2 kernel. We experimented with three different kernels—Exponential, Matérn-5/2, and Matérn-3/2, and found that the Matérn-3/2 kernel provided the best performance. Our approach guarantees feasibility of $\hat{B}_k(X, I)$; see similar projections for machine-learning emulators (Exarchos et al., 2018; Sage et al., 2024). The complete SHADOW-GP procedure is outlined in Algorithm 1. Recall that $\bar{\mathcal{D}}_k^v$ is the design \mathcal{D}_k^v without replicates. Here, $\mathcal{N}_{loc} = \{1, 2, \dots, N_{loc}\}$, $\mathcal{N}_{rep} = \{1, 2, \dots, N_{rep}\}$, and $\mathcal{N}_b = \{1, 2, \dots, N_b\}$.

Estimating the value function: After training, Algorithm 1 yields continuation-value emulators $\{\hat{Q}_k(\cdot)\}_{k=1}^{K-1}$ and optimal control emulators $\{\hat{B}_k(\cdot)\}_{k=0}^{K-1}$. To evaluate the resulting hybrid resource output trajectory (O_k) and the respective value function, we utilize Monte Carlo simulation.

Given an initial state (X_0, I_0) , we generate M out-of-sample paths $(X_{0:K}^m, I_{0:K}^{*,m})$, $m = 1, \dots, M$, where the optimized SoC $I_{k+1}^{*,m}$ is based on $\hat{b}_k^m := \hat{B}_k(X_k^m, I_k^{*,m})$ evaluated from (37). This gives cumulative pathwise realized cost

$$v_{0:K}^m = \sum_{k=0}^{K-1} f(X_k^m, \hat{b}_k^m, M_k) + g(I_T^{*,m}), \quad (38)$$

and the resulting Monte Carlo estimate of the value function:

$$\hat{V}(0, X_0, I_0) = \frac{1}{M} \sum_{m=1}^M v_{0:K}^m. \quad (39)$$

Algorithm 1 Stochastic hybrid asset dispatch optimization with Gaussian Process (SHADow-GP)

- 1: **Input:** K steps, N_{loc} sites, N_{rep} replications, N_b numerical optimizations per step.
 - 2: Set $\hat{Q}_{K-1}(X, I) = g(I)$ (No emulation)
 - 3: **for** $k = K - 1$ to 0 **do**
 - 4: Generate training design $\mathcal{D}_k^b = \{(X_k^{b,i}, I_k^{b,i}), i \in \mathcal{N}_b\}$.
 - 5: Optimize $b_k^{\dagger,i}$ in (34) pointwise for each $(X_k^{b,i}, I_k^{b,i})$ for $i \in \mathcal{N}_b$.
 - 6: Fit control GP $\tilde{B}_k(\cdot)$ according to (36) using $b_k^{\dagger,i}$ and $(X_k^{b,i}, I_k^{b,i})$ for $i \in \mathcal{N}_b$.
 - 7: **if** $k \neq 0$ **then**
 - 8: Generate replicated training design $\mathcal{D}_{k-1}^v = \{(X_{k-1}^{i,j}, I_k^{i,j}), i \in \mathcal{N}_{loc} \text{ and } j \in \mathcal{N}_{rep}\}$.
 - 9: Generate one-step paths: $X_{k-1}^{i,j} \mapsto X_k^{i,j}$ for $i \in \mathcal{N}_{loc}$ and $j \in \mathcal{N}_{rep}$.
 - 10: Evaluate $\hat{b}_k^{i,j}$ according to (37) using $\tilde{B}_k(\cdot)$ on $(X_k^{i,j}, I_k^{i,j})$ for $i \in \mathcal{N}_{loc}$ and $j \in \mathcal{N}_{rep}$.
 - 11: Evaluate $v_k^{i,j}$ in (24) for $i \in \mathcal{N}_{loc}$ and $j \in \mathcal{N}_{rep}$.
 - 12: Average over replicates: $\bar{v}_k^n = \frac{1}{N_{rep}} \sum_{j=1}^{N_{rep}} v_k^{n,j}$ for $n \in \mathcal{N}_{loc}$
 - 13: Fit continuation-value GP $\hat{Q}_{k-1}(\cdot)$, according to (26), by regressing \bar{v}_k^n against (X_{k-1}^n, I_k^n) in reduced design $\tilde{\mathcal{D}}_{k-1}^v$ for $n \in \mathcal{N}_{loc}$.
 - 14: **end if**
 - 15: **end for**
- Output:** q -value emulators $\{\hat{Q}_k(\cdot)\}_{k=1}^{K-1}$ and control emulators $\{\hat{B}_k(\cdot)\}_{k=0}^{K-1}$
-

3.5 Case Study with Stationary Dynamics

We utilize the analytical solution from Proposition 1 to provide a baseline against our SHADow-GP algorithm. We consider quarter-hour increments $\Delta t = 1/4$ with time-stationary generation with a constant dispatch target, $M_k \equiv 5$ MW for $k = 0, \dots, 95$. The parameters of the stationary Jacobi process and BESS are listed in Table 1. Minimum generation is set to $X_{\min} = 0$ and maximum generation is $X_{\max} = 10$ MW. Our choice of B_{\max} and B_{\min} implies that the charge / discharge capacity can handle deviations up to $1 \text{ StDev}(X_k) = 1$ MW away from the dispatch target of 5 MW. We take a 3-hour battery with $I_{\max} = 3B_{\max} = 3$ MWh (Department of Market Monitoring, 2024). In our simulations, the BESS starts with 50% SoC, $I_0 = 1.5$ MW; accordingly the terminal condition is $g(t) = \mathcal{P}(t - I_{\text{target}})^2$ with $\mathcal{P} = 10$ and $I_{\text{target}} = 1.5$ MW.

$\alpha_k = 0.5$	$m_k = 5$ (MW)	$\sigma_k = 0.2$ (hr^{-1})
$SoC_{\min} = 0$	$SoC_{\max} = 1$	$I_{\max} = 3$ (MWh)
$B_{\min} = -1$ (MW)	$B_{\max} = 1$ (MW)	$\eta = 1$

Table 1: Parameters for the stationary example in Sect. 3.5

To train GP emulators $\{\hat{B}_k(\cdot), \hat{Q}_k(\cdot)\}_{k=0}^{95}$, we use a Latin Hypercube Sampling (LHS) training design \mathcal{D}_k^v and \mathcal{D}_k^b of size $N = N_{loc} \times N_{rep} = 3.2 \times 10^4$ and $N_b = N_{loc}$ respectively at each time step k , with $N_{loc} = 640$ sites and batch size $N_{rep} = 50$. Here, 40 of the N_{loc} design points come from the fencing of the boundary of sampling domain. The implementation of SHADow-GP uses the Python `scikit` library run on a MacBook Pro M1 laptop with 16GB RAM and an Apple M1 8-core CPU. The computation takes approximately 15 minutes.

The left panel of Figure 2 visualizes the resulting policy $\hat{B}_{GP,k}(\cdot, \cdot)$ for our SHADow-GP algorithm at $k = 0$, based on the quadratic running cost (7). Observe that when SoC is far from empty or full, $\hat{B}_{GP,0}(X, I) \simeq X - M_0$ is almost linear in the middle of the policy surface. However, when both the SoC I and renewable generation X are high, the optimal control decreases the charging rate $\hat{B}_{GP,0}(X, I) < X - M_0$ to maintain SoC headroom. Similarly, the controller throttles the BESS discharging when the SoC is very low. As a result, over the day I_k^* tends to stay in a “safe zone” and away from SoC limits, demonstrating precautionary risk mitigation behavior.

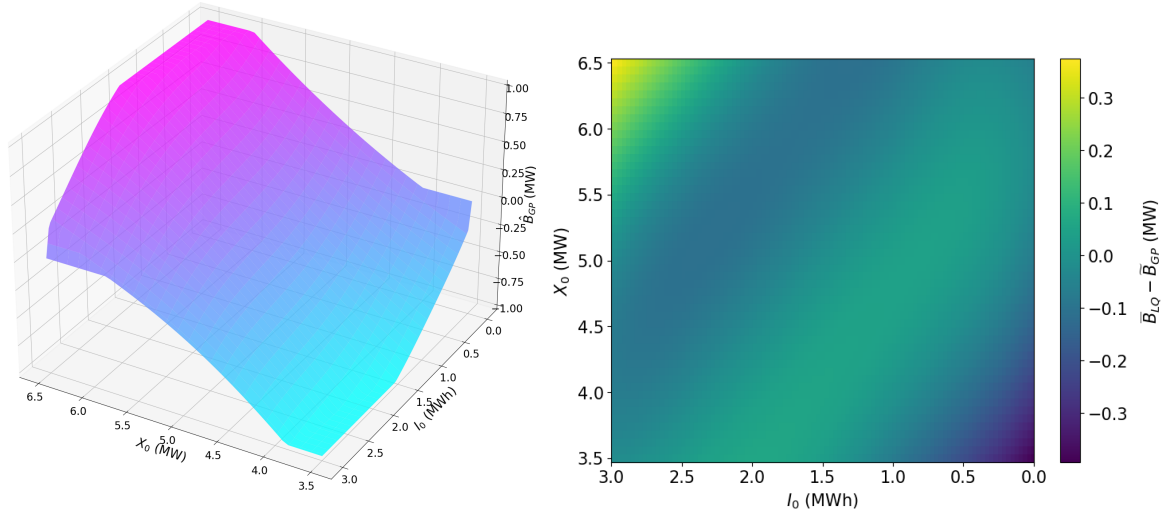


Figure 2: *Left panel:* Learned control policy $(X, I) \mapsto \hat{B}_{GP,k}(X, I)$ for the setting of Section 3.5 at $k = 0$ as a function of SoC I and wind generation X . The dispatch target is $M_0 = 5$ MW. *Right panel:* Difference between the LQ and GP-based controls without power and capacity constraints, $\bar{B}_{LQ,0}(X, I) - \check{B}_{GP,0}(X, I)$ at $k = 0$.

Next, we compare our SHADow-GP algorithm with the closed-form LQ approximation of Prop. 1 that yields strategy $\bar{B}_{LQ,k}(X, I)$. Thanks to the symmetry of the terminal cost with our quadratic penalization on SoC in (13) and $M_k = m_k$, our optimal control in Prop. 1 simplifies to

$$\bar{B}_{LQ,k}(X, I; c_1, c_2) = -\kappa P_1(t_k) \cdot (I - I_m) + \frac{\kappa}{2}(2 - P_2(t_k)) \cdot (X - m). \quad (40)$$

To make a fair comparison between the two strategies, we optimize the pair (c_1, c_2) from (11) with respect to the running cost (7). That is, we compute the value function in (39) using $\bar{B}_{LQ,k}(\cdot; c_1, c_2)$, manually projected onto \mathcal{B}_k , using 10,000 Monte Carlo trajectories. This procedure is repeated in the grid $[0, 10] \times [0, 10]$, with increments of $\Delta c_1 = \Delta c_2 = 0.01$. We find that $c_1^* = 0.08$ and $c_2^* = 0.06$ yield the lowest cumulative cost, with a 4-6% increase in cumulative cost compared to SHADow-GP. The difference in optimal controls between SHADow-GP and LQ with these c_1^*, c_2^* is shown in the right panel of Figure 2. The SHADow-GP charges/discharges less than the LQ strategy with increasing/decreasing SoC and wind power output. In addition to the quadratic “soft” approximation of the constraints, we suspect that this discrepancy also stems from applying the continuous-time control $\bar{B}_{LQ,k}(\cdot)$ within a discrete-time framework.

The top panel of Figure 3 displays a representative 24-hour trajectory of the raw renewable generation (X_k) , relative to its firmed (O_k^{LQ}) and (O_k^{GP}) outputs based on the analytical LQ and SHADow-GP control maps. Both controllers act strategically, conserving some battery capacity rather than myopically charging/discharging to the maximum extent. As expected, larger deviations are adjusted more aggressively. The GP-based control is better at avoiding SoC limits, for instance keeping $I_k^{GP,*} > 0$ non-empty during hours 3-7 (bottom panel of Figure 3) which in turn leads to a smoother overall trajectory of (O_k^{GP}) compared to (O_k^{LQ}) .

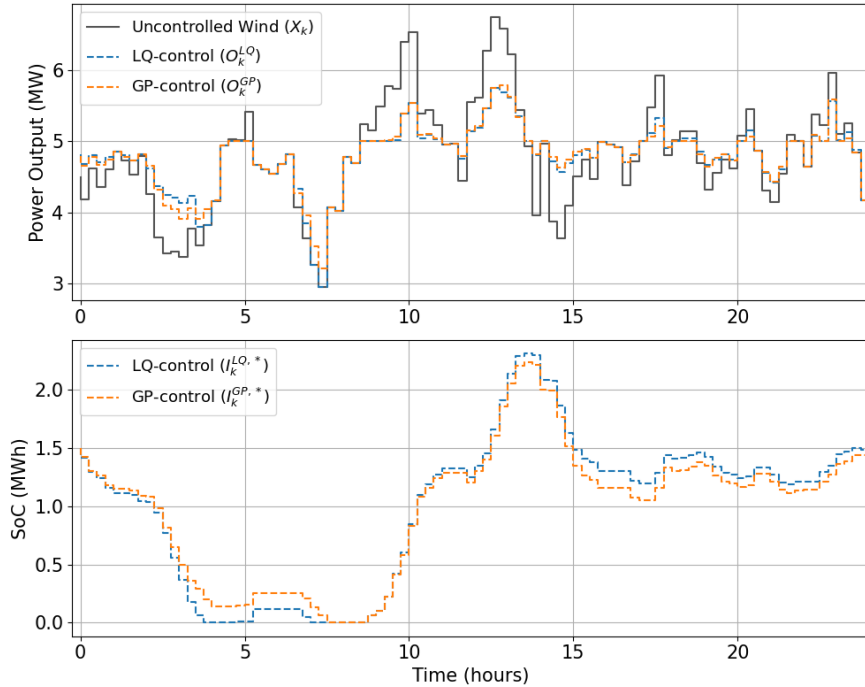


Figure 3: *Top panel:* A trajectory of (X_k) following (1) with constant mean $\mathbb{E}[X_k] = 5$ along with firmed hybrid output (O_k) following LQ and SHADow-GP controls. *Bottom panel:* Corresponding SoC trajectories $(I_k^{LQ,*})$ and $(I_k^{GP,*})$.

4 Experiments on Texas-7k grid

In this section, we evaluate the performance of our SHADow-GP algorithm under realistic grid conditions. Our experimental platform utilizes a synthetic model of the ERCOT grid, known as the Texas-7k (Birchfield, Overbye, & Davis, 2019). The grid covers the area managed by ERCOT and includes 185 renewable assets comprised of 36 solar and 149 wind units, see Figure 13 in Appendix B. None of the Texas-7k assets are hybrid, largely because the testbed was developed before the widespread adoption of BESS. Thus, we frame our study as impact analysis for a potential retrofit of existing wind farms with BESS; such retrofits are popular since they face simplified interconnection queue permitting and moreover enjoy tax breaks, enhancing their business case over new greenfield hybrid projects.

To apply SHADow-GP to Texas-7k, we first calibrate the dynamics of (X_k) to each individual unit. We then evaluate SHADow-GP in our synthetic model-based setting, hybridizing the given wind farm with a 3-hour battery and a max charge/discharge rate set to 10% of the unit’s nameplate capacity. Finally, we assess the benefit of hybridization by feeding the output (O_k^*) into a full unit-commitment and economic dispatch (ED) framework. To this end, we utilize VATIC ED optimization software suite (Grzadkowski, Fang, Yang, Solomon, & Sircar, 2023). Critically, to assess realistic firming, we use respective day-ahead forecasts as our dispatch target (M_k) and compute (O_k^*) along actual trajectories of wind generation, rather than on model-based test simulations.

4.1 Calibration of Wind Dynamics

We utilize the reanalyzed NREL data set (Xu, Birchfield, Shetye, & Overbye, 2017) for calibration of wind assets. The data set comprises hourly ($\Delta t = 1$) actual and forecasted (as of noon on the day prior) wind generation profiles in 2018 for the 149 wind units in Texas-7k, with generation capacities ranging from 30MW to 352MW. To start the calibration process, we rescale the actual and forecasted wind generation profiles of each wind farm by its nameplate capacity, obtaining respective *generation ratios* taking values in $[0, 1]$. To distinguish data from our model-based quantities, in this section we use $A_k^{\ell,d}$ to denote the observed generation ratio of asset ℓ on day d in hour k and $F_k^{\ell,d}$ the corresponding day-ahead forecast, later also used as dispatch target $M_k^{\ell,d}$.

Wind generation is driven by wind speed which exhibits diurnal variations, marked by fluctuations in both mean and variance during a 24-hour period. To incorporate these features, the drift and diffusion coefficients of (X_k) are taken to be dependent on both time-of-day and forecast. Rather than using the Jacobi SDE (1), we found that a more flexible fit is provided by forecast-dependent mean-reverting dynamics

$$X_{k+1}^{\ell,d} = X_k^{\ell,d} + \alpha(F_k^{\ell,d})(F_k^{\ell,d} - X_k^{\ell,d})\Delta t + \sigma(F_k^{\ell,d}) \cdot \epsilon_k \quad \text{for } k = 0, 1, \dots, 23, \quad (41)$$

where $F_k^{\ell,d}$ is the day-ahead forecast generation ratio for hour k on day d , and (ϵ_k) is the exogenous noise. Direct calibration of $\alpha(\cdot)$ and $\sigma(\cdot)$ as continuous functions of $F \in [0, 1]$ in (41) leads to a complex statistical optimization problem that falls beyond the scope of this paper. To simplify, we take $\alpha(\cdot)$ and $\sigma(\cdot)$ to be piecewise constant in F . Specifically, we partition the forecast values into 10 equi-probable bins and estimate α and σ independently within each bin. We first assign hourly forecasts to the bins using the non-decreasing map $R : F \subset [0, 1] \mapsto \mathbb{B} := \{1, 2, \dots, 10\}$, denoting

by $\mathcal{N}_r^\ell = \{(d, k) : R(F_k^{\ell,d}) = r\}$ the day-hour pairs that fall into bin r for asset ℓ . Since we have hourly observations for 365 days, we have $N_\ell = 8,760$ total observations and $N_r^\ell = \lfloor N_\ell/10 \rfloor = 876 \forall \ell$ observations in each bin $r \in \mathbb{B}$.

We then estimate the mean-reversion rate α_r^ℓ and volatility σ_r^ℓ in each bin $r \in \mathbb{B}$ and each asset ℓ via least squares under the dynamics of (41), following the procedure in Heymann et al. (2016); Balata et al. (2021). The bin mean-reversion rate is based on a linear regression of the next-hour increments of actual generation $(A_{k+1}^{\ell,d} - A_k^{\ell,d})$ against the current deviation $(F_k^{\ell,d} - A_k^{\ell,d})$,

$$\alpha_r^\ell = \arg \min_{\alpha \in \mathbb{R}} \sum_{(d,k) \in \mathcal{N}_r^\ell} \left((A_{k+1}^{\ell,d} - A_k^{\ell,d}) - \alpha \cdot (F_k^{\ell,d} - A_k^{\ell,d}) \right)^2;$$

and the bin volatility is the empirical standard deviation of the resulting residuals

$$\sigma_r^\ell = \text{StDev}(\mathcal{E}_r^\ell) \quad \text{where} \quad \mathcal{E}_r^\ell := \{(A_{k+1}^{\ell,d} - A_k^{\ell,d}) - \alpha_r^\ell (F_k^{\ell,d} - A_k^{\ell,d}) : (d, k) \in \mathcal{N}_r^\ell\}.$$

Figure 4 depicts a boxplot of the resulting σ_r^ℓ for $r = 1, \dots, 10$ across $\ell = 1, \dots, 149$ assets. The general pattern of σ_r^ℓ is low volatility when the forecasted generation ratio is very low or very high (a calm day with minimal wind or strong steady wind), and much higher σ_r^ℓ for generation ratios in the middle. This can be further linked to the nonlinear (approximately cubic) behavior of wind generation as a function of wind speed at intermediate speeds. Figure 15 in the Supplementary Materials shows the corresponding boxplot of α_r^ℓ 's.

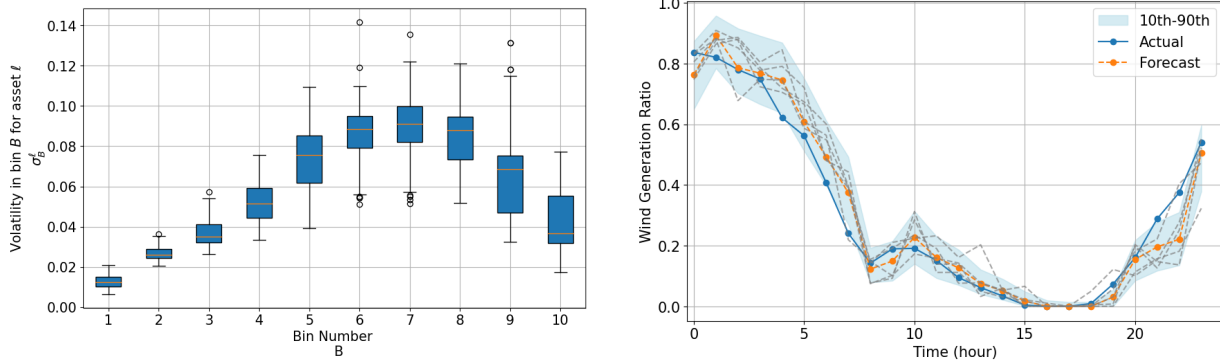


Figure 4: *Left panel:* Boxplot of the calibrated volatility σ_r^ℓ across 149 wind assets in Texas-7k, shown as a function of bin $r = 1, \dots, 10$. *Right panel:* Wind generation ratio scenarios generated by (43) for Foard City Wind Farm on 2018-04-05. The dotted lines are 5 sample hourly trajectories; the light blue band is the 80% scenario band. We also show the day-ahead forecast (orange) and the actual generation ratio on that day (blue).

It remains to specify the exogenous i.i.d. shocks ϵ_k in the calibrated dynamics:

$$X_{k+1}^{\ell,d} = X_k^{\ell,d} + \alpha_{R(F_k^{\ell,d})}^\ell (F_k^{\ell,d} - X_k^{\ell,d}) + \sigma_{R(F_k^{\ell,d})}^\ell \cdot \epsilon_k \quad \text{for } k = 0, 1, \dots, 23, \quad (42)$$

After calibrating α^ℓ, σ^ℓ , the residuals, \mathcal{E}^ℓ , across bins reveal that the shocks ϵ_k^ℓ deviate from a Gaussian distribution, cf. supplementary Figure 17 in Appendix C. In addition, we need to simultaneously constrain $X_{k+1}^{\ell,d} \in [0, 1]$ and allow for the positive probability of hitting the boundaries $[0, 1]$ which occurs frequently, especially when the forecast similarly satisfies $F_k^{\ell,d} \in \{0, 1\}$, see the actual

trajectory of the generation ratio ($A_k^{\ell,d}$) in the right panel of Figure 4. The latter is another reason why we do not use the Jacobi SDE (1) whose trajectories stay in the interior $(0, 1)$ a.s. To address these issues we make two adjustments for the distribution of (ϵ_k^ℓ) . First, we replace the Gaussian assumption with a bootstrapping approach.

$$X_{k+1}^{\ell,d} = X_k^{\ell,d} + \alpha_{R(F_k^{\ell,d})}^\ell (F_k^{\ell,d} - X_k^{\ell,d}) + \sigma_{R(F_k^{\ell,d})}^\ell \cdot \epsilon_{R(F_k^{\ell,d})}^\ell \quad \text{for } k = 0, 1, \dots, 23, \quad (43)$$

where the shocks ϵ_r^ℓ are generated by bootstrapping samples from the binned distribution of residuals \mathcal{E}_r^ℓ . Second, to maintain the trajectories of $(X_k^{\ell,d})$ within $[0, 1]$ and reach the boundaries with positive probability, we further modify our shocks ϵ_r^ℓ . In particular, consider the case when $R(F_k^{\ell,d}) = 1$, corresponding to the first decile bin. Since all forecasts within this bin are equal to zero, we have $F_k^{\ell,d} = 0$. We generate ϵ_1^ℓ by using a mixed distribution, adding a point mass at zero for ϵ_1^ℓ . To do so, we first sample $Z_1^\ell \sim 1 - \text{Bernoulli}(p_1^\ell)$ and then set

$$\epsilon_1^\ell = \begin{cases} 0, & \text{if } Z_1^\ell = 0; \\ \epsilon_1^{\ell,+}, & \text{if } Z_1^\ell = 1, \end{cases} \quad (44)$$

where $\epsilon_1^{\ell,+}$ is a positive sample from \mathcal{E}_1^ℓ . A natural estimate for the hyperparameter p_1^ℓ is $P(X_{k+1}^{\ell,d} = 0 | X_k^{\ell,d} = 0)$. Since $X_k^{\ell,d}$ is not directly available, we rely on $F_k^{\ell,d}$ which gives rise to:

$$\hat{p}_1^\ell = \frac{\sum_{(d,k) \in \mathcal{N}_1^\ell} \mathbb{1}_{\{F_k^{\ell,d}=0, F_{k+1}^{\ell,d}=0\}}}{\sum_{(d,k) \in \mathcal{N}_1^\ell} \mathbb{1}_{\{F_k^{\ell,d}=0\}}}.$$

This ensures that the simulated wind generation ratios $X_k^{\ell,d}$ are non-negative and not positively biased when $F_k^{\ell,d} = 0$. The resulting probability of zero generation \hat{p}_1^ℓ ranges from 72% to 78% across 149 Texas-7k wind units. Therefore, with high probability, our trajectories hit the boundaries when $F_k = 0$. We apply similar modification of our shocks ϵ_{10}^ℓ where $F_k^{\ell,d} = 1$. In this case, the probability of maximum generation \hat{p}_{10}^ℓ ranges from 24% to 47%. See Li and Ludkovski (2024) for related multi-site calibration.

The right panel of Figure 4 shows the simulated generation ratio trajectories of a representative wind asset, Foard City Wind Farm, on 2018-04-05. The Figure shows the forecast generation ratio ($F_k^{\ell,d}$), the actual generation ratio ($A_k^{\ell,d}$) and five simulated trajectories ($X_k^{\ell,d}$). The Figure also demonstrates the 80% scenario band, obtained via quantiles of 10,000 Monte Carlo trajectories $\mathbf{X}^{\ell,d}$ generated according to (43). Notice the narrowing band between hours 15-19 when the forecast is zero, illustrating (44). The empirical time-averaged coverage rate $\text{ECR}^{\ell,d}$ in this case is 83%, obtained via

$$\text{ECR}^{\ell,d} := \frac{1}{24} \sum_{k=0}^{23} \mathbb{1}_{(A_k^{\ell,d} \geq q_{0.1}(\mathbf{X}_k^{\ell,d}) \text{ and } A_k^{\ell,d} \leq q_{0.9}(\mathbf{X}_k^{\ell,d}))}, \quad (45)$$

where $q_\alpha(\cdot)$ denotes the α -th quantile. The averaged empirical coverage rate $\overline{\text{ECR}}^\ell = \frac{1}{365} \sum_{d=1}^{365} \text{ECR}^{\ell,d}$ ranges from 74% to 88% across the assets, see Appendix C Figure 16. Given that the theoretical nominal coverage is 80%, this suggests that the calibrated discretized SDE model performs reasonably well but exhibits some site-to-site variability.

4.2 SHADOW-GP Evaluation

To assess the impact of hybridization, we consider retrofitting the wind assets in Texas-7k with a three-hour BESS, $I_{\max} = 3B_{\max}$ with capacity $B_{\max} = 0.10$ representing 10% of the nameplate generation capacity (recall that in this section X_k is rescaled to $[0, 1]$). Our B_{\max} is slightly higher than 1 standard deviation of the hourly forecast errors, $\{A_k^{\ell,d} - F_k^{\ell,d}\}_{(d,k) \in N_t}$, which ranges between 0.05 and 0.08. The charging efficiency parameter is set to $\eta = 0.95$ for 10% round-trip losses, while $\text{SoC}_{\min} = 0.05$ and $\text{SoC}_{\max} = 0.95$, which means that the BESS has a 5% SoC buffer. Gorman et al. (2024) reports that existing wind-hybrid BESS roundtrip efficiencies, computed as the ratio of aggregate discharged energy relative to aggregate charged energy, in US are in the range 75 – 95%. We use the same simulation design as the case study in Section 3.5. We use hourly steps with $K = 24$ total steps. We utilize the same running cost \tilde{f} and terminal cost g as in the stationary example for all our experiments, with terminal penalty $\mathcal{P} = 1$, which was re-scaled to the numerical scale of I_{\max} . The rest of the section utilizes the same case study as in the previous section: Foard City Wind Farm on 2018-04-05.

The pervasive time-dependence of (X_k) makes the solution, i.e. the maps \hat{Q}_k, \hat{B}_k also strongly dependent on k . The SHADOW-GP algorithm automatically adapts the training domain (\mathcal{D}_k^v) at each step k to reflect the time-varying distribution of (X_k) , see the x -axes in Figure 5 that shows $\bar{\mathcal{D}}_k^v$ at two different hours. Figure 5 also illustrates the (kernel-smoothed) density of 10,000 Monte Carlo trajectories of optimally dispatched (X_k, I_k^*) at $k = 2$ and $k = 6$. The supplementary Figure 18 plots the differences between the respective control maps at those two hours.

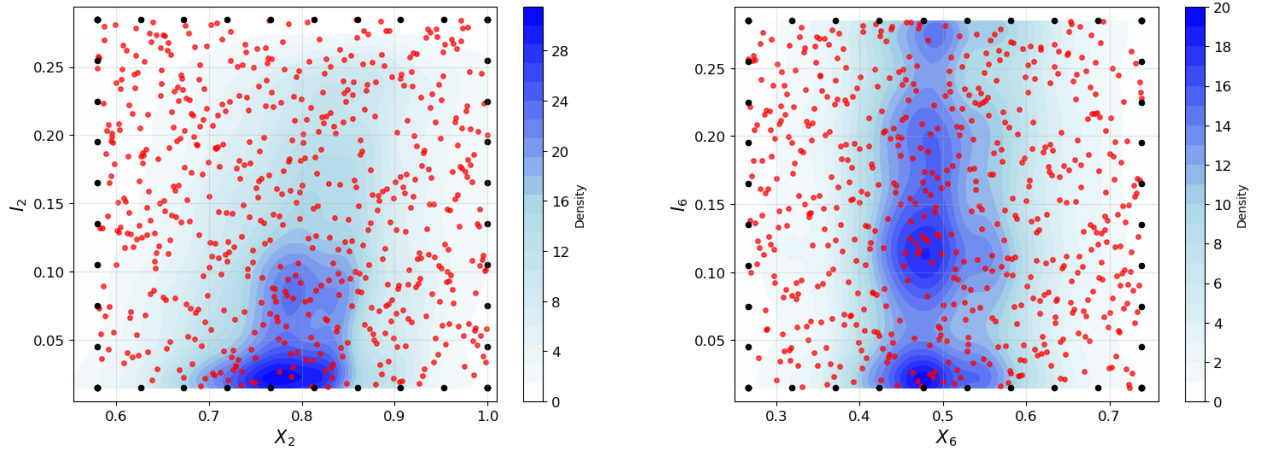


Figure 5: Simulation design $\bar{\mathcal{D}}_k^v$ of size $N_{loc} = 600$ for the model calibrated to Foard City Wind Farm. We use LHS on the indicated time-dependent adaptive rectangular training domain; the 40 black dots represent the fencing mechanism. The colors indicate the (kernel-based) density of resulting optimized trajectories (X_k, I_k^*) . *Left panel:* $k = 2$. *Right panel:* $k = 6$.

Finally, Figure 6 compares the 80% confidence interval of dispatch deviation without BESS $(X_k - F_k)$ and with BESS $(O_k - F_k)$. As expected, with BESS, we have a tighter band around the target. Notice that the distance between the outer band and the inner band is always less than B_{\max} due to the SoC constraints and the objective \tilde{f} .

Next, we analyze the results of SHADOW-GP on all wind assets. To do so, we introduce the

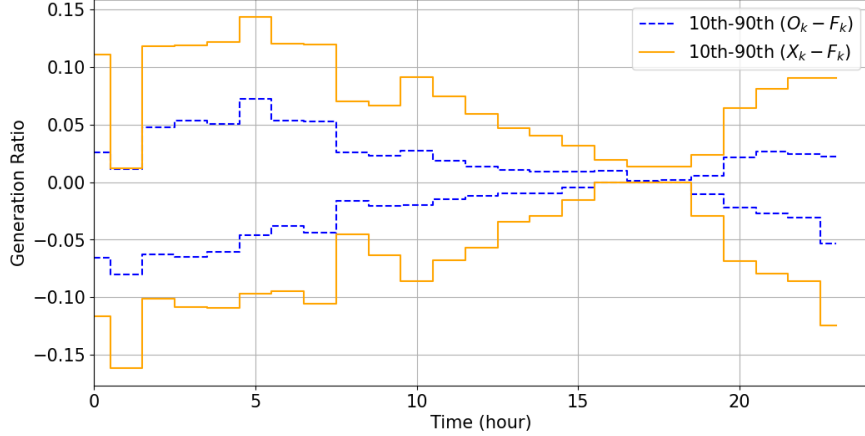


Figure 6: Standalone and hybridized dispatch deviations for Foard City Wind Farm. The y -axis is centered around the dispatch target, so perfect match corresponds to zero deviation. Orange solid/blue dotted lines represents the 80% confidence interval of dispatch deviation without BESS ($X_k - F_k$) and after optimal BESS firming ($O_k - F_k$). The confidence intervals are based on 10,000 Monte Carlo trajectories with SHADow-GP control.

Deviation Reduction (DR) metric in units (%) for a given asset ℓ :

$$\text{DR}^{\ell,d} := \left(\frac{\text{Dev}(A^{\ell,d}) - \text{Dev}(O^{*,\ell,d})}{\text{Dev}(A^{\ell,d})} \right) \times 100\% \quad (46)$$

where d is the test day, $O^{*,\ell,d}$ is the the profile after firming $A^{\ell,d}$ and for any $Z^{\ell,d} = (Z_k^{\ell,d})$, $\text{Dev}(Z^{\ell,d}) := \sum_{k=0}^{23} |Z_k^{\ell,d} - F_k^{\ell,d}|$ is the total daily deviation of the profile Z from target generation ratio. We proceed by training our algorithm for 24 randomly selected test days, 2 days from each month. Since we have 149 hybrid assets, this totals to 149×24 runs of SHADow-GP, each run taking ≈ 5 minutes. Figure 7 visualizes the averaged $\overline{\text{DR}}^\ell = \frac{1}{24} \sum_{d=1}^{24} \text{DR}^{\ell,d}$ over the test days for the 149 wind assets in Texas-7k. We observe $\overline{\text{DR}}^\ell$ as low as 40% and as high as 67%, with a clear spatial pattern whereby higher reductions are observed in the southern and southeastern Texas, as indicated by the brighter yellow bubbles, which also correspond to larger hybrid assets. We observe lowest $\overline{\text{DR}}^\ell$ (%) in the Far North region of ERCOT.

4.3 Benefits of Hybridization

In this section we provide an economic assessment of the benefits of retrofitting wind assets with BESS by integrating the SHADow-GP algorithm with grid simulation and optimization software, **Vatic**. **Vatic** is a framework that replicates the operation of the power generation network over a designated study period to identify the optimal set of operational decisions to meet demand at minimal cost (Grzadkowski et al., 2023). **Vatic** employs a two-step process, which is repeated for each day of the study period, see Figure 8. First, the Unit Commitment (UC) step schedules dispatchable generators to be on or off. The UC is generated one day ahead based on forecasts $(F_k^{\ell,d}), \ell = 1, \dots, 149$, producing the 24-hour UC schedule. During the subsequent Economic Dispatch step, **Vatic** sets the hourly generation ratio for all active dispatchable generators based

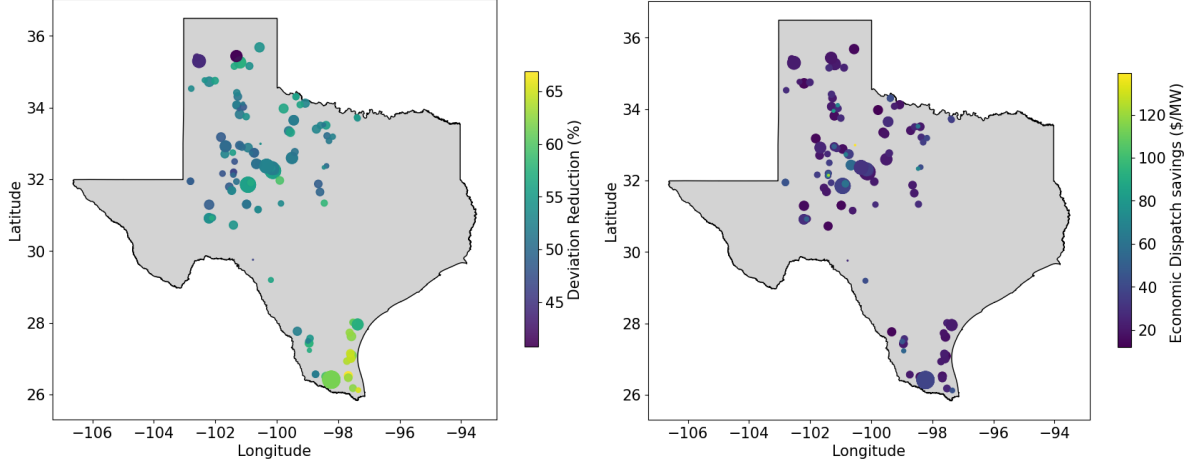


Figure 7: *Left panel*: average percentage deviation reduction \overline{DR}^ℓ from hybridization for the 149 wind assets in Texas-7k. *Right panel*: respective Economic Dispatch (ED) daily savings in dollars per MW. Symbol size is proportional to nameplate generation capacity.

on actual load and renewable generation and the forecasted quantities for the next two hours. In **Vatic** real-time ED is solved to minimize generation costs and uses a 20% reserve margin. For each operational day, SHADOW-GP takes as input the forecast and actual generation ratios, returning firmed generation ($O_k^{*,\ell,d}$). Afterwards, **Vatic** takes ($O_k^{*,\ell,d}$) and ($F_k^{\ell,d}$) scaled back into MW units, performs ED, and produces operational summary statistics for the relevant variables.

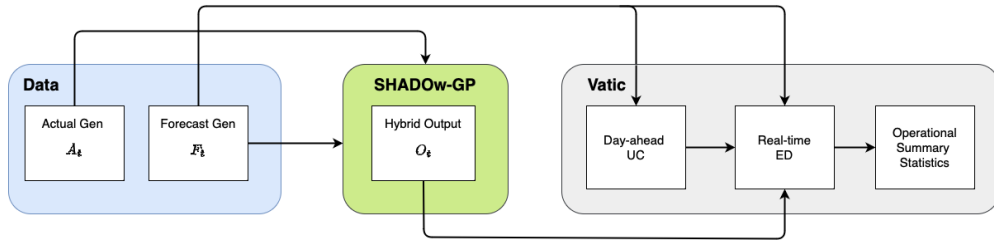


Figure 8: Integration of SHADOW-GP for Economic Dispatch in **Vatic**.

For each hybrid asset, we run **Vatic** with hybrid output ($O_k^{*,\ell,d}$) for the same $D = 24$ test days in the previous section, resulting in 149×24 individual runs. Here, we emphasize that we turn only one wind asset into a hybrid for each run. We utilize the same BESS parameters as in the previous section for each hybrid. In addition, we perform a base run with only wind output ($A_k^{\ell,d}$) instead of hybrid output ($O_k^{*,\ell,d}$), resulting in additional 24 runs. The right panel of Figure 7 reports the ED savings in dollars per MW for each asset ℓ ,

$$\text{ED savings}^\ell := \frac{\sum_{d=1}^D \left(\text{ED}_d^{\text{Base}} - \text{ED}_d^{\text{Hybrid},\ell} \right)}{D \cdot B_{\max} \times \bar{C}_\ell} \quad (47)$$

where $\text{ED}_d^{\text{Base}}$ is the daily variable generation cost (\$) of the grid in the base run without hybrid

assets on day d and $\text{ED}_d^{\text{Hybrid},\ell}$ is the cost for the grid with asset ℓ hybridized. To account for asset nameplate capacities, we normalize by $B_{\max} \times \bar{C}_\ell$ the power rating (MW) of the battery in asset ℓ .

We observe savings on average of 30 \$/MW. In addition, it is interesting to see that small hybrid assets can bring as high as 140 \$/MW of ED savings. Note that the ED savings in Figure 7 do not have a one-to-one correspondence with DR (%). In other words, $\text{Dev}(O^{\ell,d}) < \text{Dev}(A^{\ell,d})$ does not guarantee lower ED costs. ED costs depend on other factors, such as actual and forecast load, available generators, and line congestion.

Remark 6. *We also ran the ED optimization with increasing number of hybrid assets using 3-hour BESSs to assess the curtailment reduction. The curtailments are visualized in Appendix B.*

4.4 BESS duration

BESS duration is among the key parameters affecting firming performance. Larger energy capacity allows the hybrid asset to sustain target generation level even in the face of a prolonged deviation. Typical durations, which in our model correspond to the ratio I_{\max}/B_{\max} , are 1–6 hours, with 2-hour and 4-hour durations being the most common configurations for Lithium-ion battery storage circa 2025.

To quantify the benefit to the grid of installing a longer-duration battery we compare firming performance when we change from the 3-hour BESS ($I_{\max}/B_{\max} = 3$) of the previous section to a larger 6-hour BESS ($I_{\max}/B_{\max} = 6$). For this analysis, we maintain the same power rating with $B_{\max} = 10\%$ of the nameplate capacity; an alternative could be to de-rate the BESS capacity to say consider $B_{\max} = 5\%$ and $I_{\max} = 0.3$ which however would be more difficult to interpret as it would lead to countervailing impacts of lower capacity vis-a-vis higher duration.

Figure 9 visualizes the gains in terms of higher DR (more firming) from using a longer duration battery. We re-run VATIC ED, making 149×24 new runs as each potential hybrid retrofit is individually adjusted to $I_{\max} = 0.6$. We observe gains of 6-13% with longer-duration batteries. The intuition would be that gains are linked to the frequency of situations where more energy capacity is needed to charge/discharge over 3+ hours due to the particular wind generation remaining consistently above/below the forecast for several successive hours.

5 Alternative objectives

5.1 Greedy Objective

The quadratic firming criterion (7) used so far leads to a smooth relationship between $B_k(X, I)$ and SoC I . In contrast, a greedy controller engages in immediate charging or discharging without any foresight. To demonstrate this, we introduce the L_1 objective:

$$f_{L_1}(X_k, B_k, M_k) := |X_k - B_k - M_k|. \quad (48)$$

L_1 -optimal control is less explored than quadratic L_2 -optimal control due to the non-smoothness of the objective, which leads to more complex control structures. Without state constraints, the optimal control can be shown to follow a *bang-off-bang* structure (Exarchos et al., 2018; Nagahara

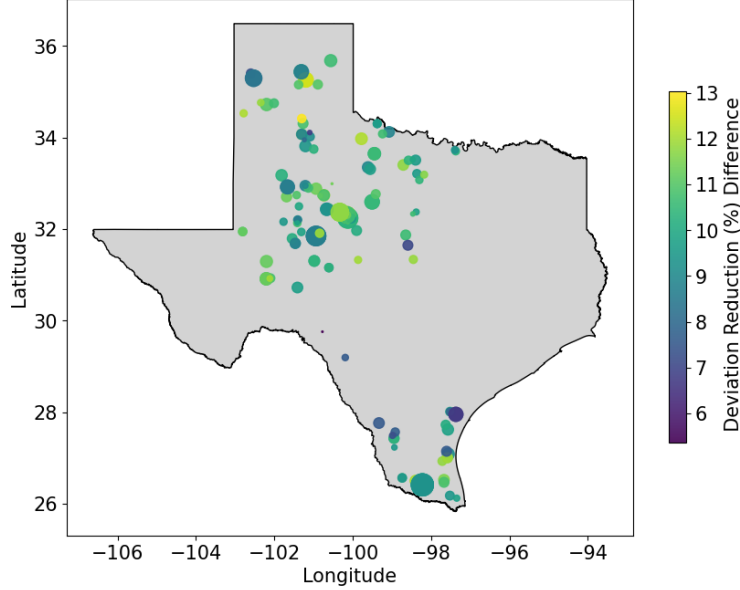


Figure 9: Improved firming performance (measured as additional reduction in DR) for an individual wind asset hybrid retrofit using a 6-hour BESS vis-a-vis a 3-hour BESS. We show the 149 wind assets in the Texas-7k grid, color-coded by average percentage reduction in DR across 24 test days. Symbol size is proportional to nameplate generation capacity.

et al., 2013). In the context of our objective (48), the optimal control $B_k^{L_1}(X_k, I_k)$ takes two values: $X_k - M_k$ or 0, subject to state-dependent constraints $\mathcal{B}_k(I_k)$.

To demonstrate this numerically, we run the SHADOW-GP algorithm for cost criterion (48), for the case study of Section 4.2, utilizing the same BESS parameters. The nonsmooth absolute-value in (48) causes the objective function in (34) to be nonsmooth, increasing the run time by about a factor of $\simeq 4$ compared to the original quadratic objective, as the optimizer must numerically approximate the gradient. Figure 10 compares the paths of the re-centered firming output and the State of Charge (SoC) arising from the L_1 (48) and quadratic (7) objectives. Evidently, the L_1 objective incites the BESS to swiftly charge or discharge to promptly minimize deviations, in a *greedy* (myopic) fashion. Moreover, L_1 -costs cause the BESS to frequently be 0% or 100% full, restricting flexibility at later steps, while the quadratic objective tries to strategically maintain headroom.

5.2 Degradation-aware Firming

BESS cycling adversely affects its useful lifetime. As the battery ages, both its usable energy capacity SoC_{\max} , and its roundtrip efficiency η drop. In this section we consider a modified stepwise cost function that mitigates degradation by penalizing deep cycles. In the context of dynamic control, degradation cost functions have been used in Heymann and Martinon (2018); Abdulla et al. (2016). Physically, degradation is driven by cumulative lifetime depth-of-discharge (DoD) which is a path-dependent quantity that requires, e.g., the rainflow counting algorithm and is incompatible with dynamic programming. Consequently, we adapt the approach of Heymann and Martinon

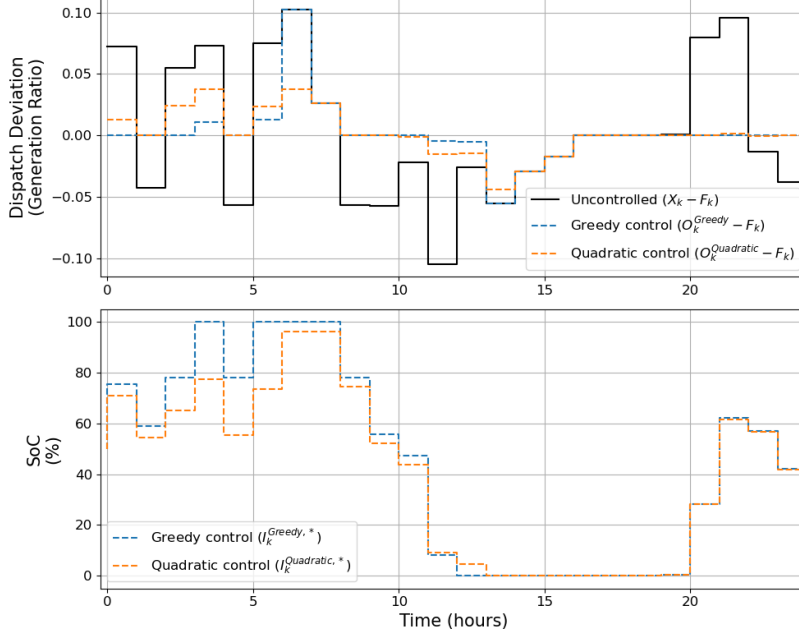


Figure 10: *Top panel:* A representative trajectory of dispatch deviation without firming ($X_k - F_k$) and with firming ($O_k - F_k$), the latter based on \tilde{f} (quadratic control) or f_{L_1} (greedy control). *Bottom panel:* Corresponding SoC trajectories (I_k^*) optimizing \tilde{f} and f_{L_1} .

(2018), modeling degradation as a nonlinear function of the SoC and the charge/discharge rate:

$$\Phi(B, I) = \left(1 - 0.5\left(\frac{I}{I_{\max}}\right)^2\right) \cdot \max(-B, 0), \quad (49)$$

leading to the modified stepwise cost function:

$$f_{BL}(X_k, B_k, M_k) := \tilde{f}(X_k, B_k, M_k) + \lambda_{BL} \cdot \Phi(B_k, I_k), \quad (50)$$

where λ_{BL} is the weight of the Battery Lifetime penalty. The second term in (49) increases as $I \downarrow I_{\min}$ or $B \downarrow B_{\min}$ penalizing discharges of nearly empty battery that are associated with high DoD. By considering (50), the controller prefers more shallow cycling.

To assess the impact of our degradation proxy Φ , we evaluate battery degradation over realized dispatch trajectories after optimizing with $f_{BL}(\cdot)$. Specifically, the resulting SoC profile (I_k^*) is decomposed into charging- and discharging half-cycles using rainflow cycle counting (Shi et al., 2019). The corresponding degradation over the operational day d for asset ℓ is then calculated according to:

$$L^{\ell, d}(\mathbf{c}, \mathbf{d}) = \sum_{i=1}^{|\mathbf{c}|} \frac{\Theta(c_i)}{2} + \sum_{i=1}^{|\mathbf{d}|} \frac{\Theta(d_i)}{2}, \quad (51)$$

where \mathbf{c} (resp. \mathbf{d}) represents the depth-of-charge (depth-of-discharge) vector for the charging (discharging) half-cycles in (I_k^*) and

$$\Theta(\text{DoD}) = (5.24 \times 10^{-4}) (\text{DoD})^{2.03}. \quad (52)$$

Above, the constant up front in (52) implies that a single daily cycle of full 100% discharge followed by a full charge would lead to a BESS lifetime of $1/(5.24 \cdot 10^{-4})/365 \simeq 5.2$ years.

Figure 11 explores the performance of the controller under f_{BL} for $\lambda_{BL} \in \{0, 0.1, 0.2\}$ within the case study of Section 4.2. As expected, larger λ_{BL} values result in more muted charging and discharging rates in response to departures from the dispatch target. This pattern is clear in the SoC trajectories in the bottom panel, where controllers with higher λ_{BL} show smaller SoC fluctuations. However, this benefit is offset by larger deviations ($O_k - F_k$), as illustrated in Figure 11.

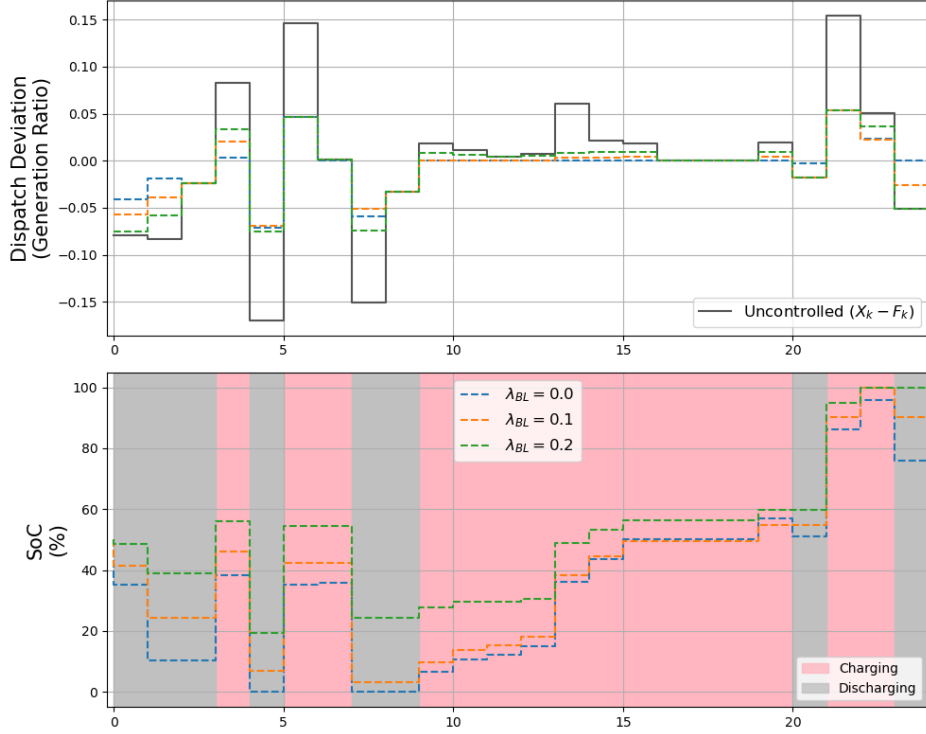


Figure 11: *Top panel:* A representative trajectory of dispatch deviation without firming ($X_k - F_k$) and with firming ($O_k - F_k$) over one day $k = 0, \dots, 23$. *Bottom panel:* Corresponding firmed SoC trajectories I_k^* . We show three scenarios based on battery lifetime penalty $\lambda_{BL} \in \{0, 0.1, 0.2\}$.

To illustrate, we deploy SHADOW-GP within the framework of f_{BL} across $\lambda_{BL} \in \{0, 0.02, 0.04, \dots, 0.2\}$; higher λ_{BL} places greater emphasis on minimizing Φ . Consequently, as λ_{BL} is increased, we anticipate observing a reduction in firming performance and an extension in battery lifespan. In this spirit, we introduce the Expected Battery Life (EBL) metric, measured in years:

$$\text{EBL}^{\ell,d} := \mathbb{E} \left[L^{\ell,d}(\mathbf{c}, \mathbf{d})^{-1} \right]. \quad (53)$$

We re-use (54) to define Expected Deviation Reduction (EDR) percentage for operational day d :

$$\text{EDR}^{\ell,d} := \mathbb{E} \left[\frac{\text{Dev}(X^{\ell,d}) - \text{Dev}(O^{\ell,d})}{\text{Dev}(X^{\ell,d})} \right] \times 100\%. \quad (54)$$

The left panel of Figure 12 shows a nearly linear change in EBL and EDR as a function of λ_{BL} ; both expectations $\mathbb{E}[\cdot]$ are based on 10^4 Monte Carlo simulations for the representative day: Foard City Wind Farm on 2018-04-05. The results indicate that thanks to more shallow cycles, the BESS lifetime more than doubles from approximately 5 years when $\lambda_{BL} = 0$ to roughly 12 years when

$\lambda_{BL} = 0.2$. As trade-off, this entails an approximately 25% reduction in EDR performance. The linear pattern of EBL as a function of λ_{BL} implies that our proxy DoD cost Φ provides a good approximation for the rainflow-based degradation $L^{\ell,d}(\cdot)$ while avoiding the need to introduce new state variables to keep track of DoD.

5.3 Curtailment Mitigation

In this section we consider a controller that simultaneously wishes to minimize the firming performance criterion (7), as well as the asymmetric criterion of minimizing Expected Cumulative Violation (ECV) with respect to thresholds $(\overline{M}_k^{\ell,d})$:

$$\text{ECV}^{\ell,d} = \mathbb{E} \left[\sum_{k=0}^{23} \max(X_k^{\ell,d} - B_k^{\ell,d} - \overline{M}_k^{\ell,d}, 0) \right]. \quad (55)$$

One motivation for the latter objective is curtailment mitigation: avoiding excess generation that might lead to forced output reduction by the grid operator. Curtailment has been a common feature in grids with high share of renewables and is driven by over-generation and limited headroom to regulate down, leading to wasted energy and ultimately additional costs. See e.g. Rogers (2020) for wind turbine curtailment using dynamic programming.

We interpret the exogenously given $(\overline{M}_k^{\ell,d})$ as the curtailment threshold, so that (55) proxies the aggregate energy curtailed over the day. Alternatively, a constant $\overline{M}^{\ell,d}$ arises in the context of transmission line capacity limits at the point of interconnection (POI) for the hybrid asset. According to Gorman et al. (2024), some hybrid assets are oversized relative to POI limits, so that $\overline{M}^{\ell,d} < 1$ and the BESS must be charging when renewable output is close to its nameplate capacity.

The controller aims to optimally redirect any generation above \overline{M}_k towards BESS, while continuing to firm towards the dispatch target $M_k \leq \overline{M}_k$, leading to the Curtailment Mitigation (CM) stepwise cost criterion:

$$f_{\text{CM}}(X_k, B_k, M_k) := \tilde{f}(X_k, B_k, M_k) + \lambda_{\text{CM}} \cdot \max(X_k - B_k - \overline{M}_k, 0). \quad (56)$$

The right panel of Figure 12 demonstrates the trade-off between firming and violation costs, EDR and ECV respectively, for a range of weights $\lambda_{\text{CM}} \in [0, 1]$, setting $\overline{M}_k := 1.05 \cdot M_k$ i.e., 5% above the dispatch target M_k . The relationship between ECV and λ_{CM} is highly non-linear with a significant change between $\lambda_{\text{CM}} = 0$ and $\lambda_{\text{CM}} = 0.2$. We observe that taking $\lambda_{\text{CM}} = 1$ results in a 40% decrease in ECV compared to $\lambda_{\text{CM}} = 0$, trading off for only 6% decrease in EDR performance, suggesting that the cost criterion f_{CM} does a good job at peak shaving.

6 Conclusion and Future Work

We developed an algorithm for the dynamic real-time dispatch of a hybrid wind asset. Our framework works with continuous state and action spaces in a closed-loop fashion and effectively handles many performance objectives, such as quadratic penalty firming, degradation-aware firming, and curtailment reduction. The implementation is moreover independent of the underlying dynamics of (X_k) and can be adjusted to use nonparametric scenario simulators. In addition, the accuracy of

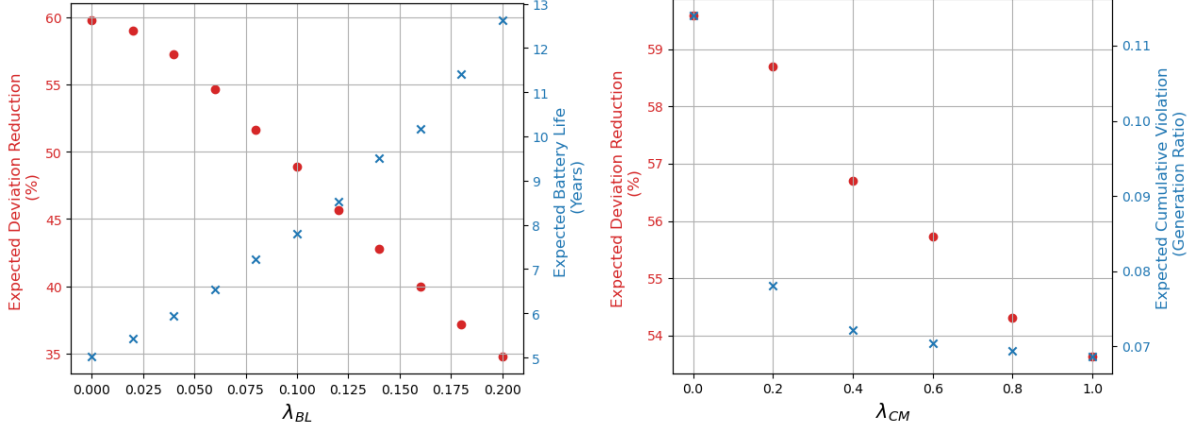


Figure 12: *Left panel:* Trade-off between EDR and EBL, evaluated for $\lambda_{BL} \in \{0, 0.02, 0.04, \dots, 0.2\}$ for objective BL in (50). *Right panel:* Trade-off between EDR and ECV, evaluated for $\lambda_{CM} \in \{0, 0.2, \dots, 1.0\}$ for objective CM in (55). For both panels, the metrics are computed via 10^4 Monte Carlo trajectories on Foard City Wind Farm, 2018-04-05.

our optimal control was validated by comparing it with an analytical solution in the linear-quadratic subcase. Furthermore, we provided a case study of our algorithm through experiments conducted on a synthetic Texas-7k grid.

Our proposed algorithm controls the BESS under the assumption of constant penalty for deviation from the target profile (M_k). In practice, the penalty for missing the dispatch targets (M_k) depends on real-time electricity prices (P_k). Therefore, a hybrid controller might employ a time-sensitive firming strategy where the firming goal aligns with P_k . A natural extension would be to perform price-dependent firming by introducing an additional state variable (P_k) to (19):

$$V(t_k, X_k, I_k, P_k) = \inf_{B_k \in \mathcal{B}_k} \left\{ f(X_k, B_k, M_k, P_k) + \mathbb{E} [V(t_{k+1}, X_{k+1}, I_{k+1}(B_k), P_{k+1}) | X_k, I_k, P_k] \right\} \quad (57)$$

where f is a price-dependent firming criterion, such as $f(x, b, m, p) = p(x - b - m)^2$.

The presented model focuses solely on real-time dispatch tracking of hybrid assets. In a different vein, these assets can be active in both the day-ahead (DA) and real-time (RT) markets. Therefore, a hybrid asset can first strategically participate in the DA market, and then dynamically adjust their positions via RT market during the operational day. This leads to a two-step optimization in which RT adjustments are impacted by earlier DA commitments, and can be recast as a firming objective where the target (M_t) is itself optimized (via a different objective) based on the day-ahead prices, see Collet et al. (2018). Full co-optimization across the DA and RT markets would require to capture the probabilistic relationship between DA and RT prices.

From a control perspective, an important generalization would be to adapt our control emulator \hat{B} to a multivariate control setting with constraints, which would open the door to study BESS use-case stacking, such as the hybrid asset jointly participating in firming and ancillary service provision.

References

- Abdulla, K., De Hoog, J., Muenzel, V., Suits, F., Steer, K., Wirth, A., & Halgamuge, S. (2016). Optimal operation of energy storage systems considering forecasts and battery degradation. *IEEE Transactions on Smart Grid*, *9*(3), 2086–2096.
- Abi Jaber, E., De Carvalho, N., & Pham, H. (2024). *Trading with propagators and constraints: applications to optimal execution and battery storage*. (arXiv:2409.12098)
- Ahlstrom, M., Mays, J., Gimon, E., Gelston, A., Murphy, C., Denholm, P., & Nemet, G. (2021). Hybrid resources: Challenges, implications, opportunities, and innovation. *IEEE Power and Energy Magazine*, *19*(6), 37–44. doi: 10.1109/MPE.2021.3104077
- Alasseur, C., Balata, A., Aziza, S., Maheshwari, A., Tankov, P., & Warin, X. (2019, 02). Regression Monte Carlo for microgrid management. *ESAIM: Proceedings and Surveys*, *65*, 46–67. doi: <https://doi.org/10.1051/proc/201965046>
- Arteaga, J., & Zareipour, H. (2019). A price-maker/price-taker model for the operation of battery storage systems in electricity markets. *IEEE Transactions on Smart Grid*, *10*(6), 6912–6920. doi: 10.1109/TSG.2019.2913818
- Aung, T., & Ludkovski, M. (2024). Optimal dispatch of hybrid renewable–battery storage resources: A stochastic control approach. In *2024 IEEE 63rd Conference on Decision and Control (CDC)* (pp. 2182–2188). doi: <https://doi.org/10.1109/CDC56724.2024.10886540>
- Bachouch, A., Huré, C., Langrené, N., & Pham, H. (2022). Deep neural networks algorithms for stochastic control problems on finite horizon: Numerical applications. *Methodology and Computing in Applied Probability*, *24*(1), 143–178. doi: <https://doi.org/10.1007/s11009-019-09767-9>
- Balata, A., Ludkovski, M., Maheshwari, A., & Palczewski, J. (2021). Statistical learning for probability-constrained stochastic optimal control. *European Journal of Operational Research*, *290*(2), 640–656. doi: <https://doi.org/10.1016/j.ejor.2020.08.041>
- Belloni, A., Piroddi, L., & Prandini, M. (2016). A stochastic optimal control solution to the energy management of a microgrid with storage and renewables. In *2016 American Control Conference (ACC)* (pp. 2340–2345). doi: 10.1109/ACC.2016.7525267
- Bermúdez, A., & Padín, I. (2024, 02). Stochastic control with state constraints via the Fokker–Planck equation. application to renewable energy plants with batteries. *Comptes Rendus. Mécanique*, *351*, 1–22. doi: <https://doi.org/10.5802/crmeca.236>
- Birchfield, A. B., Overbye, T. J., & Davis, K. R. (2019). Educational applications of large synthetic power grids. *IEEE Transactions on Power Systems*, *34*(1), 765–772. doi: 10.1109/TPWRS.2018.2859910
- Caballero, R., Kebaier, A., Scavino, M., & Tempone, R. (2021). Quantifying uncertainty with a derivative tracking SDE model and application to wind power forecast data. *Statistics and Computing*, *31*(5), 64. doi: <https://doi.org/10.1007/s11222-021-10040-8>
- Collet, J., Féron, O., & Tankov, P. (2018). Optimal management of a wind power plant with storage capacity. In P. Drobinski, M. Mougeot, D. Picard, R. Plougonven, & P. Tankov (Eds.), *Renewable energy: Forecasting and risk management* (pp. 229–246). Cham: Springer International Publishing.

- Department of Market Monitoring. (2024). *2023 special report on battery storage* (Tech. Rep.). CAISO.
- Ding, H., Hu, Z., & Song, Y. (2012). Stochastic optimization of the daily operation of wind farm and pumped-hydro-storage plant. *Renewable Energy*, *48*, 571–578. doi: <https://doi.org/10.1016/j.renene.2012.06.008>
- Donti, P. L., Rolnick, D., & Kolter, J. Z. (2021). *DC3: A learning method for optimization with hard constraints*. (arXiv:2104.12225)
- Drissi, F. (2022, November). Solvability of differential Riccati equations and applications to algorithmic trading with signals. *Applied Mathematical Finance*, *29*(6), 457–493. doi: <http://dx.doi.org/10.1080/1350486x.2023.2241130>
- Exarchos, I., Theodorou, E. A., & Tsiotras, P. (2018, August). Stochastic l_1 -optimal control via forward and backward sampling. *Systems & Control Letters*, *118*, 101–108. doi: <https://doi.org/10.1016/j.sysconle.2018.06.005>
- Gorman, W., Rand, J., Manderlink, N., Cheyette, A., Bolinger, M., Seel, J., ... Wiser, R. (2024). *Hybrid power plants: Status of operating and proposed plants, 2024 edition* (Tech. Rep.). Lawrence Berkeley National Lab. Retrieved from <https://emp.lbl.gov/hybrid>
- Grzadkowski, M., Fang, J. A., Yang, X., Solomon, A., & Sircar, R. (2023, September). *Princetonuniversity/vatic: Texas-7k 2030 and python 3.11*. Zenodo. doi: <https://doi.org/10.5281/zenodo.8381228>
- Han, J., & Hu, R. (2020). *Deep fictitious play for finding Markovian Nash equilibrium in multi-agent games*. (arXiv:1912.01809)
- He, G., Chen, Q., Kang, C., Pinson, P., & Xia, Q. (2016). Optimal bidding strategy of battery storage in power markets considering performance-based regulation and battery cycle life. *IEEE Transactions on Smart Grid*, *7*(5), 2359–2367. doi: [10.1109/TSG.2015.2424314](https://doi.org/10.1109/TSG.2015.2424314)
- Heymann, B., Bonnans, J. F., Silva, F., & Jimenez, G. (2016). A stochastic continuous time model for microgrid energy management. In *2016 european control conference (ecc)* (pp. 2084–2089). doi: <https://doi.org/10.1109/ECC.2016.7810599>
- Heymann, B., & Martinon, P. (2018, 08). Optimal battery aging: An adaptive weights dynamic programming algorithm. *Journal of Optimization Theory and Applications*, *179*, 1043–1053. doi: <https://doi.org/10.1007/s10957-018-1371-9>
- Hybrid Resources Task Force. (2022). *Unlocking the flexibility of hybrid resources* (Tech. Rep.). Reston, VA: Energy Systems Integration Group.
- Johnson, P., Howell, S., & Duck, P. (2017, July). Partial differential equation methods for stochastic dynamic optimization: an application to wind power generation with energy storage. *Philosophical Transactions of the Royal Society A: Mathematical, Physical and Engineering Sciences*, *375*(2100). (Publisher: Royal Society) doi: <https://doi.org/10.1098/rsta.2016.0301>
- Khalid, M., & Savkin, A. (2010). A model predictive control approach to the problem of wind power smoothing with controlled battery storage. *Renewable Energy*, *35*(7), 1520–1526. (Special Section: IST National Conference 2009) doi: <https://doi.org/10.1016/j.renene.2009.11.030>
- Koller, M., Borsche, T., Ulbig, A., & Andersson, G. (2013). Defining a degradation cost function for optimal control of a battery energy storage system. In *2013 IEEE Grenoble conference* (pp. 1–6). doi: <https://doi.org/10.1109/PTC.2013.6652329>

- Kordonis, I., Charalampidis, A. C., & Haessig, P. (2023). Optimal operation of a grid-connected battery energy storage system over its lifetime. *Optimal Control Applications and Methods*, 44(2), 739–757. doi: <https://doi.org/10.1002/oca.2830>
- Kotary, J., & Fioretto, F. (2024). *Learning constrained optimization with deep augmented lagrangian methods*. (arXiv:2403.03454)
- Kotary, J., Fioretto, F., Hentenryck, P. V., & Wilder, B. (2021). *End-to-end constrained optimization learning: A survey*. (arXiv:2103.16378)
- Kou, P., Gao, F., & Guan, X. (2015). Stochastic predictive control of battery energy storage for wind farm dispatching: Using probabilistic wind power forecasts. *Renewable Energy*, 80, 286–300. doi: <https://doi.org/10.1016/j.renene.2015.02.001>
- Krishnamurthy, D., Uckun, C., Zhou, Z., Thimmapuram, P. R., & Botterud, A. (2018). Energy storage arbitrage under day-ahead and real-time price uncertainty. *IEEE Transactions on Power Systems*, 33(1), 84–93. doi: 10.1109/TPWRS.2017.2685347
- Lee, J.-O., & Kim, Y.-S. (2022). Novel battery degradation cost formulation for optimal scheduling of battery energy storage systems. *International Journal of Electrical Power & Energy Systems*, 137, 107795. doi: <https://doi.org/10.1016/j.ijepes.2021.107795>
- Li, Q., & Ludkovski, M. (2024). *Probabilistic spatiotemporal modeling of day-ahead wind power generation with input-warped Gaussian processes*. (arXiv:2409.16308)
- Ludkovski, M., & Maheshwari, A. (2020, 05). Simulation methods for stochastic storage problems: A statistical learning perspective. *Energy Systems*, 11, 377–415. doi: <https://doi.org/10.1007/s12667-018-0318-4>
- Møller, J. K., Zugno, M., & Madsen, H. (2016). Probabilistic forecasts of wind power generation by stochastic differential equation models. *Journal of Forecasting*, 35(3), 189–205. doi: <https://doi.org/10.1002/for.2367>
- Muenzel, V., de Hoog, J., Brazil, M., Vishwanath, A., & Kalyanaraman, S. (2015). A multi-factor battery cycle life prediction methodology for optimal battery management. New York, NY, USA: Association for Computing Machinery. doi: 10.1145/2768510.2768532
- Nagahara, M., Quevedo, D. E., & Nesić, D. (2013). *Maximum-hands-off control and L1 optimality*. (arXiv:1307.8232)
- North American Electric Reliability Corporation. (2021, December). *Grid forming technology: Bulk power system reliability considerations* (Tech. Rep.). North American Electric Reliability Corporation (NERC). Retrieved from https://www.nerc.com/comm/RSTC_Reliability_Guidelines/White_Paper_Grid_Forming_Technology.pdf
- Oskouei, M. Z., & Yazdankhah, A. S. (2015). Scenario-based stochastic optimal operation of wind, photovoltaic, pump-storage hybrid system in frequency- based pricing. *Energy Conversion and Management*, 105, 1105–1114. doi: <https://doi.org/10.1016/j.enconman.2015.08.062>
- Pham, H. (2009). *Continuous-time stochastic control and optimization with financial applications*. Springer Berlin Heidelberg. doi: 10.1007/978-3-540-89500-8
- Rasmussen, C. E., & Williams, C. K. I. (2006). *Gaussian processes for machine learning*. MIT Press.
- Rogers, J. (2020). Optimal strategies for wind turbine environmental curtailment. *Wind Energy*, 23(5), 1331–1350. doi: <https://doi.org/10.1002/we.2489>

- Sage, M., Campbell, J., & Zhao, Y. F. (2024, July). Enhancing battery storage energy arbitrage with deep reinforcement learning and time-series forecasting. In *Asme 2024 18th international conference on energy sustainability*. American Society of Mechanical Engineers. doi: <https://doi.org/10.1115/es2024-130538>
- Shi, Y., Xu, B., Tan, Y., Kirschen, D., & Zhang, B. (2019). Optimal battery control under cycle aging mechanisms in pay for performance settings. *IEEE Transactions on Automatic Control*, *64*(6), 2324–2339. doi: [10.1109/TAC.2018.2867507](https://doi.org/10.1109/TAC.2018.2867507)
- Sirignano, J., & Spiliopoulos, K. (2018, December). DGM: a deep learning algorithm for solving partial differential equations. *Journal of Computational Physics*, *375*, 1339–1364. doi: <https://doi.org/10.1016/j.jcp.2018.08.029>
- US Energy Information Administration. (2024). *Utilities report batteries are mos commonly used for arbitrage and grid stability* (Tech. Rep.). (Today in Energy: In-brief analysis (June 25, 2024))
- van der Meer, D., Wang, G. C., & Munkhammar, J. (2021). An alternative optimal strategy for stochastic model predictive control of a residential battery energy management system with solar photovoltaic. *Applied Energy*, *283*, 116289. doi: <https://doi.org/10.1016/j.apenergy.2020.116289>
- Wu, D., Jin, C., Balducci, P., & Kintner-Meyer, M. (2015). An energy storage assessment: Using optimal control strategies to capture multiple services. In *2015 IEEE Power & Energy Society General Meeting* (pp. 1–5). doi: [10.1109/PESGM.2015.7285820](https://doi.org/10.1109/PESGM.2015.7285820)
- Xu, T., Birchfield, A. B., Shetye, K. S., & Overbye, T. J. (2017). Creation of synthetic electric grid models for transient stability studies. In *The 10th Bulk Power Systems Dynamics and Control Symposium (IREP 2017)* (pp. 1–6).
- Zheng, N., Liu, X., Xu, B., & Shi, Y. (2023). Energy storage price arbitrage via opportunity value function prediction. In *2023 IEEE Power & Energy Society General Meeting* (pp. 1–5). doi: [10.1109/PESGM52003.2023.10253102](https://doi.org/10.1109/PESGM52003.2023.10253102)

Supplementary Materials

A Proof of Proposition 1

The unconstrained HJB equation in Section 2.4 Proposition 1 is given by:

$$\partial_t \bar{V} + \inf_{\bar{b} \in \mathcal{R}} \left\{ \alpha_t(m-x) \partial_X \bar{V} + \bar{b} \partial_I \bar{V} + \frac{1}{2} \sigma_t^2 x \cdot (X_{\max} - x) \partial_{XX} \bar{V} + (x - \bar{b} - M_t)^2 + c_1 \bar{b}^2 + c_2 (\iota - I_m)^2 \right\} = 0, \quad (58)$$

with terminal condition $\bar{V}(T, x, \iota) = \mathcal{P}(\iota - I_{\text{target}})^2$. Since the value function is quadratic in x, ι with interaction terms, we can derive an analytical formulation for the optimal control and \bar{V} .

The first-order condition of \bar{b} in (58) is:

$$\bar{b} = \kappa(x - M_t) - \frac{\kappa}{2} (\partial_I \bar{V}), \quad (59)$$

where $\kappa = \frac{1}{1+c_1}$. Plugging back into (58) yields

$$\begin{aligned} \partial_t \bar{V} + \alpha_t(m-x) \partial_X \bar{V} + \left[\kappa(x - M_t) - \frac{\kappa}{2} \partial_I \bar{V} \right] \partial_I \bar{V} + \frac{1}{2} \sigma_t^2 x \cdot (X_{\max} - x) \partial_{XX} \bar{V} + \\ \left[(x - M_t) - \kappa(x - M_t) + \frac{\kappa}{2} \partial_I \bar{V} \right]^2 + c_1 \left[\kappa(x - M_t) - \frac{\kappa}{2} (\partial_I \bar{V}) \right]^2 + c_2 (\iota - I_m)^2 = 0. \end{aligned}$$

Expanding and simplifying we end up with

$$\partial_t \bar{V} + (1 - \kappa)(x - M_t)^2 + c_2(\iota - I_m)^2 - \alpha_t(x - m) \partial_X \bar{V} + \kappa(x - M_t) \partial_I \bar{V} - \frac{\kappa}{4} (\partial_I \bar{V})^2 + \frac{1}{2} \sigma_t^2 \partial_{XX} \bar{V} = 0.$$

We rewrite $x - M_t = (x - m) + (m - M_t)$ to yield:

$$\begin{aligned} \partial_t \bar{V} + (1 - \kappa)(x - m)^2 + 2(1 - \kappa)(m - M_t)(x - m) + (1 - \kappa)(m - M_t)^2 \\ + c_2(\iota - I_m)^2 - \alpha_t(x - m) \partial_X \bar{V} + \kappa(x - m) \partial_I \bar{V} + \kappa(m - M_t) \partial_I \bar{V} \\ - \frac{\kappa}{4} (\partial_I \bar{V})^2 + \frac{1}{2} \sigma_t^2 x \cdot (X_{\max} - x) \partial_{XX} \bar{V} = 0. \end{aligned}$$

We solve the PDE by proposing the ansatz

$$\begin{aligned} \bar{V}(t, x, \iota) = P_1(t)(\iota - I_m)^2 + P_2(t)(\iota - I_m)(x - m) + P_3(t)(x - m)^2 \\ + P_4(t)(\iota - I_m) + P_5(t)(x - m) + P_6(t) \end{aligned} \quad (60)$$

for functions of time $P_j(t), j = 1, \dots, 6$ to be determined. Substituting back and gathering terms we get

$$\begin{aligned} \dot{P}_1(t)(\iota - I_m)^2 + \dot{P}_2(t)(\iota - I_m)(x - m) + \dot{P}_3(t)(x - m)^2 + \dot{P}_4(t)(\iota - I_m) + \dot{P}_5(t)(x - m) + \dot{P}_6(t) \\ + (1 - \kappa)(x - m)^2 + 2(1 - \kappa)(m - M_t)(x - m) + (1 - \kappa)(m - M_t)^2 + c_2(\iota - I_m)^2 \\ - \alpha_t(x - m) [P_2(t)(\iota - I_m) + 2P_3(t)(x - m) + P_5(t)] \\ + \kappa(x - m) [2P_1(t)(\iota - I_m) + P_2(t)(x - m) + P_4(t)] \\ + \kappa(m - M_t) [2P_1(t)(\iota - I_m) + P_2(t)(x - m) + P_4(t)] \\ - \frac{\kappa}{4} (2P_1(t)(\iota - I_m) + P_2(t)(x - m) + P_4(t))^2 + \sigma_t^2 P_3(t) x \cdot (X_{\max} - x) = 0. \end{aligned}$$

Since the basis $\{(x - m)^2, (x - m)(\iota - I_m), (\iota - I_m)^2, (x - m), (\iota - I_m), 1\}$ is linearly independent, we must have the respective coefficients identically zero, which yields the system of Riccati ODEs for $P_1(t), \dots, P_6(t)$ on $t \in [0, T]$ in (15).

The terminal condition of the ODEs above are found by matching with terminal cost $g(\iota) = \mathcal{P}(\iota - \iota_{\text{target}})^2$. By solving the ODEs, we get the analytical form of our value function (60). See Drissi (2022) for resolvability of differential Riccati systems. The optimal control is of the form:

$$\bar{b}(t, x, \iota) = \kappa(x - M_t) - \kappa P_1(t)(\iota - I_m) - \frac{\kappa}{2} P_2(t)(x - m) - \frac{\kappa}{2} P_4(t). \quad (61)$$

Remark 7. When $I_{\text{target}} = I_m$ and $\tilde{m}_k = m$, the linear terms in \bar{V} disappear as P_4 and P_5 become degenerate. The solution to the optimal control problem in this case can be found in Section 3.5. When $M_t = m$ only, the linear term with respect to $(x - m)$ in \bar{V} disappears. However, in the case $\iota_{\text{target}} = \iota_m$ only, none of the terms simplify due to the presence of $\kappa(m - M_t)\partial_I V$ in the PDE.

B Appendix: Additional Figures for Texas-7k Case Study

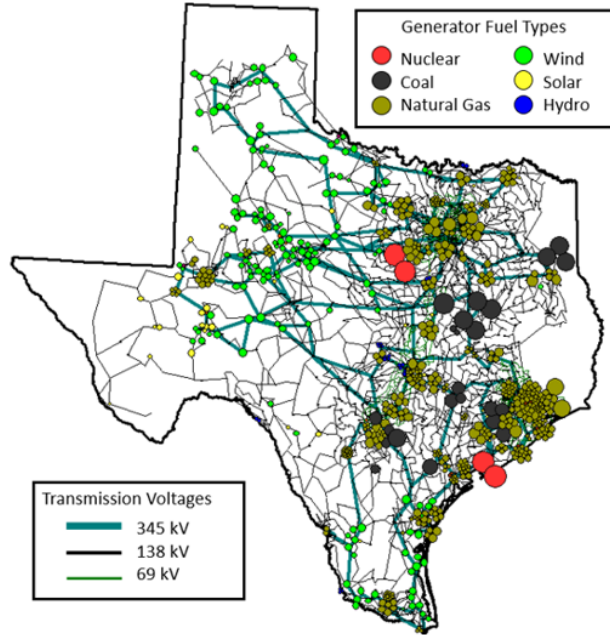


Figure 13: Topology of Texas-7k power grid. The grid transmission network consists of 7,173 lines and 1,967 transformers. There are 36 solar, 149 wind and 542 thermal generators (nuclear, coal, natural gas, etc.).

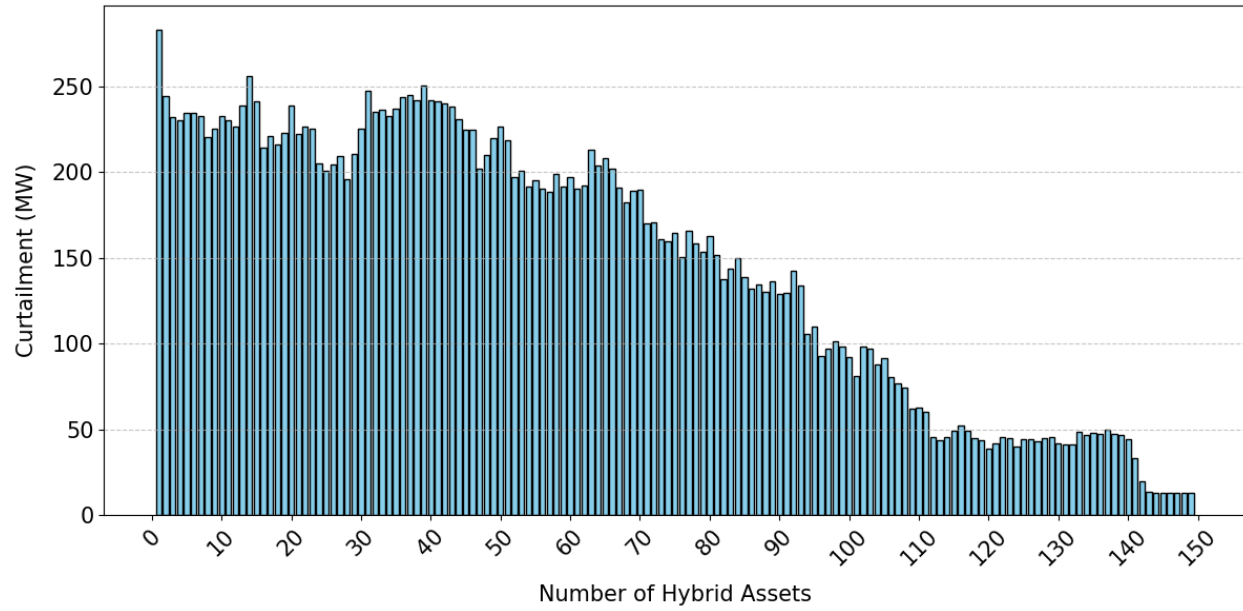


Figure 14: Total curtailment (MW) accumulated over 24 representative days as a function of the number of hybrid assets.

C Appendix: Calibration figures

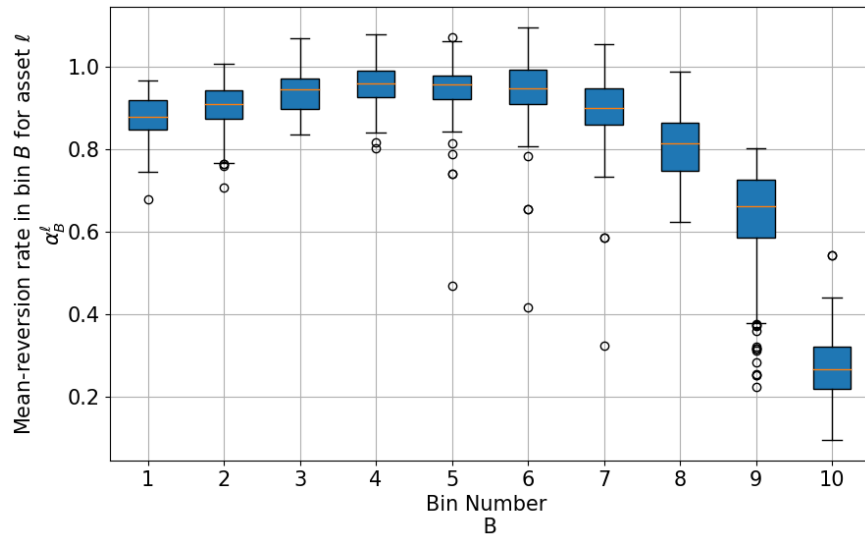


Figure 15: Boxplot of the calibrated mean-reversion rates α_r^l across 149 wind assets in Texas-7k as a function of bin $r = 1, 2, \dots, 10$.

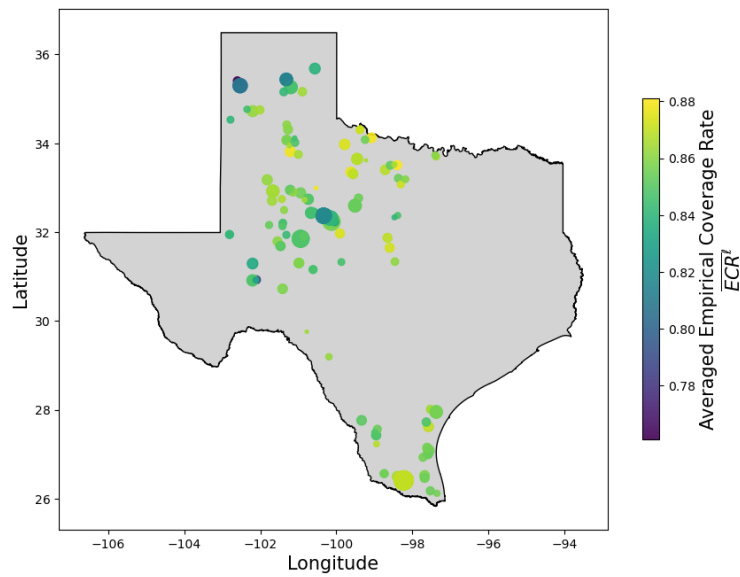


Figure 16: Averaged empirical coverage rate \overline{ECR}^l for wind assets $\ell = 1, 2, \dots, 149$ in Texas-7k. Symbol size is proportional to nameplate generation capacity.

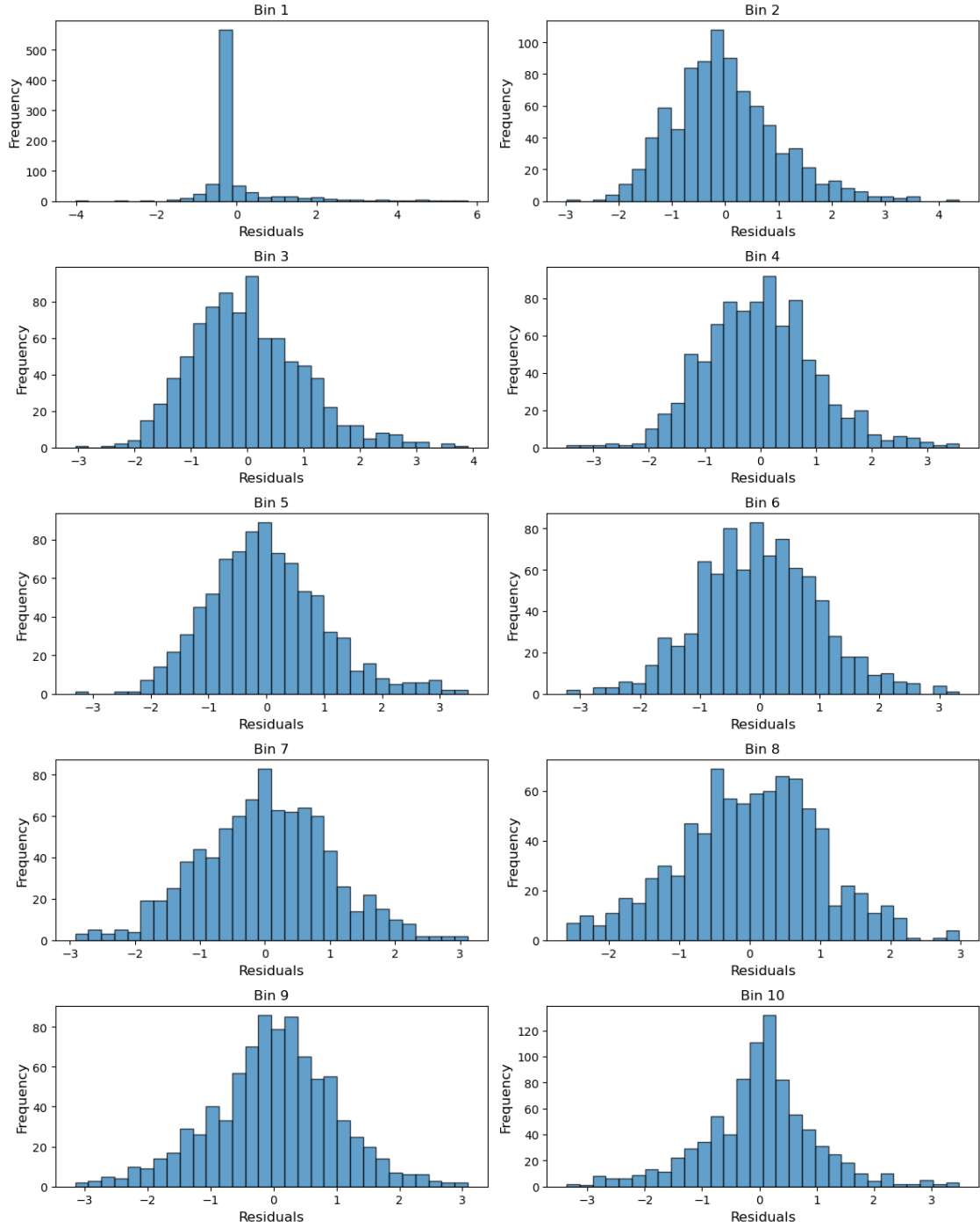


Figure 17: Bin-wise residuals after calibrating α_r and σ_r for Foard City Wind Unit across bins $r = 1, 2, \dots, 10$.

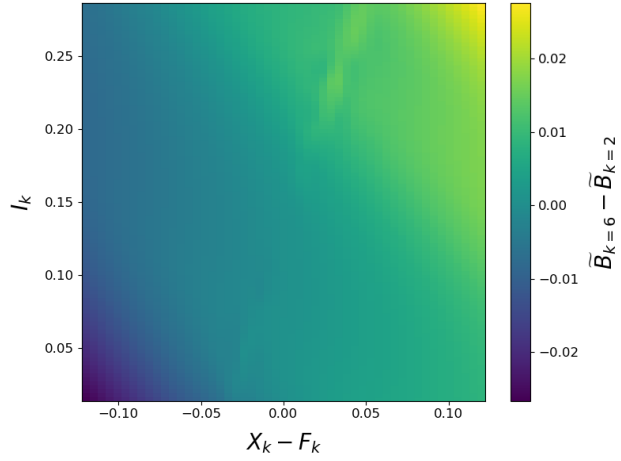


Figure 18: Difference of unconstrained optimal control policies, $\tilde{B}_k(\cdot)$, from SHADow-GP at different times, $k = 6$ and $k = 2$ as a function of (X, I) , calibrated to Foard City Wind Farm on 2018-04-05. For better visualization of deviation levels, we plot the dispatch deviation $X_k - F_k$ rather than the generation ratio X_k itself. We observe that the BESS charges/discharges more at hour $k = 6$ than at $k = 2$, demonstrating time-dependent control behavior.